

RESEARCH ARTICLE | AUGUST 02 2016

High fidelity simulation and analysis of liquid jet atomization in a gaseous crossflow at intermediate Weber numbers

Xiaoyi Li; Marios C. Soteriou



Physics of Fluids 28, 082101 (2016)
<https://doi.org/10.1063/1.4959290>



Articles You May Be Interested In

Review of atomization characteristics of liquid jets in crossflow

Physics of Fluids (February 2024)

Detailed analysis on primary and secondary break up characteristics of liquid fuel jet in crossflow using homogeneous mixture model and large eddy simulation

Physics of Fluids (November 2024)

Study on the spray characteristics of transverse jets with elliptical nozzles in supersonic crossflows using the volume of fluid–discrete phase model

Physics of Fluids (August 2024)

High fidelity simulation and analysis of liquid jet atomization in a gaseous crossflow at intermediate Weber numbers

Xiaoyi Li^{a)} and Marios C. Soteriou

United Technologies Research Center, East Hartford, Connecticut 06108, USA

(Received 8 April 2016; accepted 11 July 2016; published online 2 August 2016)

Recent advances in numerical methods coupled with the substantial enhancements in computing power and the advent of high performance computing have presented first principle, high fidelity simulation as a viable tool in the prediction and analysis of spray atomization processes. The credibility and potential impact of such simulations, however, has been hampered by the relative absence of detailed validation against experimental evidence. The numerical stability and accuracy challenges arising from the need to simulate the high liquid-gas density ratio across the sharp interfaces encountered in these flows are key reasons for this. In this work we challenge this status quo by presenting a numerical model able to deal with these challenges, employing it in simulations of liquid jet in crossflow atomization and performing extensive validation of its results against a carefully executed experiment with detailed measurements in the atomization region. We then proceed to the detailed analysis of the flow physics. The computational model employs the coupled level set and volume of fluid approach to directly capture the spatiotemporal evolution of the liquid-gas interface and the sharp-interface ghost fluid method to stably handle high liquid-air density ratio. Adaptive mesh refinement and Lagrangian droplet models are shown to be viable options for computational cost reduction. Moreover, high performance computing is leveraged to manage the computational cost. The experiment selected for validation eliminates the impact of inlet liquid and gas turbulence and focuses on the impact of the crossflow aerodynamic forces on the atomization physics. Validation is demonstrated by comparing column surface wavelengths, deformation, breakup locations, column trajectories and droplet sizes, velocities, and mass rates for a range of intermediate Weber numbers. Analysis of the physics is performed in terms of the instability and breakup characteristics and the features of downstream flow recirculation, and vortex shedding. Formation of “A” shape windward column waves is observed and explained by the combined upward and lateral surface motion. The existence of Rayleigh-Taylor instability as the primary mechanism for the windward column waves is verified for this case by comparing wavelengths from the simulations to those predicted by linear stability analyses. Physical arguments are employed to postulate that the type of instability manifested may be related to conditions such as the gas Weber number and the inlet turbulence level. The decreased column wavelength with increasing Weber number is found to cause enhanced surface stripping and early depletion of liquid core at higher Weber number. A peculiar “three-streak-two-membrane” liquid structure is identified at the lowest Weber number and explained as the consequence of the symmetric recirculation zones behind the jet column. It is found that the vortical flow downstream of the liquid column resembles a von Karman vortex street and that the coupling between the gas flow and droplet transport is weak for the conditions explored. *Published by AIP Publishing.* [<http://dx.doi.org/10.1063/1.4959290>]

^{a)}Author to whom correspondence should be addressed. Electronic mail: lixy2@utrc.utc.com

I. INTRODUCTION

Atomization of fuel jets in cross-flowing air to generate micron-size droplets is critical to the performance of combustors encountered in commercial and military aerospace applications, such as gas turbines, augmentors, scramjets and ramjets, and rockets.¹ Increased fuel area-to-volume ratio due to atomization significantly enhances the fuel evaporation rate, which contributes to better fuel-air mixing and subsequent combustion of fuels. While the magnitude of fuel-air ratio has an impact on engine efficiency and emissions, the spatiotemporal distribution of fuel vapor is strongly linked to dynamic stability.² The impact of small changes in the atomization step can be significantly amplified in the flow and reaction processes downstream. In contrast to other atomization approaches such as pressure atomization, the crossflow atomization reduces the possibilities for injection clogging.³ Therefore, substantial demand exists for the quantitative understanding of liquid atomization in crossflow, as a first step in the optimization of typical aero-engine combustion processes.

From the breakup of centimeter-size liquid jet column to pinch-off of micron-size ligaments to form droplets, liquid primary atomization in crossflow manifests itself as a complex multiphysics and multiscale phenomenon. Different dynamic forces due to gas flow, liquid inertia, and surface tension compete with each other, controlling the various instabilities that tend to characterize multiphase flows. Near the liquid column, either Rayleigh-Taylor (R-T) instability due to density difference and fluid acceleration, or Kelvin-Helmholtz (K-H) instability due to aerodynamic shear, or the combination of both drives the large scale growth of surface waves and liquid breakup.⁴⁻⁷ At a turbulent injection condition, the development of convective Kelvin-Helmholtz instability may be further amplified by introducing initial perturbations at the interface due to liquid turbulence. Jet breakup may also occur as a direct result of turbulent liquid jetting.⁸ On the other hand, capillary plateau-Rayleigh instability due to surface tension, which is active everywhere on the liquid surface, starts to play a dominant role in the pinch-off of highly stretched thin ligaments when their size drops below a certain threshold. Different instability mechanisms selectively dominate the breakup process at different flow conditions, and these have been classified phenomenologically in regimes, namely column breakup, bag breakup, multimode breakup, and shear breakup.^{4,9} In addition, various instabilities often occur simultaneously¹⁰ at different spatial locations of the column, similar to the multiple-instability scenarios encountered in liquid jet atomization in a co-flow air.¹¹ As a result, complicated location-specific liquid structures form which critically control the formation and spatial distribution of the resulting droplets. The transport and evaporation of these droplets controls the downstream fuel-air profile and hence the subsequent reacting flow.

Early experimental studies of primary atomization¹²⁻¹⁵ focused on large-scale, integral and steady features such as penetration length or liquid column trajectory, mainly because of the limitations of optical techniques in resolving the spatiotemporal evolution of the highly unsteady dense spray field. Recently, several groups started to use the pulsed shadowgraph^{1,4,9} and ballistic imaging techniques¹⁶⁻¹⁸ to obtain more details of the evolution of the liquid column. Despite the fact that most analyses are based on processing two-dimensional images, near-field features such as column wavelength, deformation of column, onset of liquid breakup, and deflected trajectory of the column were successfully extracted. The breakup of the jet column was found similar to the well-studied secondary breakup of drops due to shock wave disturbance,^{19,20} and the data were summarized in a series of correlations.^{4,9} It is worth noting that most experimental studies were conducted at ambient conditions. Data for realistic combustor operating conditions are more valuable since fluid properties (such as density, viscosity, and surface tension) and therefore the breakup processes are highly sensitive to these conditions.²¹ However, the extremely hostile high-temperature high-pressure environment in aerospace applications makes experimental research prohibitively difficult and costly.

Due to the limited scientific understandings of the complex atomization physics, in the past phenomenological models have been developed to lump the physics into simple correlations without tracking the detailed multi-scale flow and liquid-surface evolutions. The cost is low for many such phenomenological models, including Taylor analogy breakup²² and wave breakup²³ models as well as their refined descendants.²⁴ However, since experimental data must be available *a priori* for calibrating these models, they are not generic and truly predictive, and their applicability in the

non-calibrated operating conditions has been severely questioned. Alternatively, the Large Eddy Simulation (LES) approach has been applied to resolve large scale spray features^{25–31} to a certain degree of success. However, the development of physically sound two-phase sub-models to account for subgrid small-scale processes is still challenging. For example, Herrmann³² pointed out that one way to overcome such challenges and close subgrid LES terms is through fully resolved subgrid scale interface geometry, as compared to other approaches, such as Euler-Lagrangian Spray Atomization (ELSA) approach,²⁷ where direct link with subgrid scale processes is not clear.

With the increase in computational power and advancement of interface tracking/capturing methods, direct numerical simulations have shown promise in predicting detailed atomization without resorting to two-phase sub-grid filters or experimental calibrations. Methods to directly track or capture the dynamic liquid-gas interface and its topological changes include level-set (LS),^{33–35} volume-of-fluid (VOF),^{36,37} and front-tracking (FT),^{38,39} as well as their descendants, such as the refined level-set grid (RLSG) method,⁴⁰ the Hybrid LSM and Mars (HLSM) method,⁴¹ and the Coupled Level-Set and Volume-Of-Fluid (CLSVOF) method.^{30,42,43} Detailed exploration of atomization mechanisms including instability development and ligament/droplet formation has been attempted^{44,45} and the majority of simulation efforts have focused on the case of straight jet injected into quiescent air mainly applicable to diesel engine applications. However, simulating jet atomization at realistic high density ratio ($\sim 10^3$) at ambient conditions where most experimental data were obtained remains a grand challenge for most of these methods.^{5,46–48} Because of such computational challenges combined with the high cost of atomization simulations, most of these numerical algorithms, including the recent ones with enhanced treatment for high-density ratio,^{49–52} were verified in simple canonical tests only and then directly applied to simulate complicated atomization cases without detailed experimental confirmation.

In the past, we have developed a hybrid Eulerian-Lagrangian computational solver^{53,54} which combines the CLSVOF/ghost-fluid approach developed by Sussman *et al.*⁴² for the simulation of the liquid-gas interface with traditional Lagrangian droplet transport algorithms. The two approaches are coupled with modified versions of Herrmann's coupling algorithms⁵⁵ and are optimized for executions on high performance computers.⁵⁶ Since 2010, we have utilized this hybrid solver to study high density-ratio liquid jet in crossflow atomization under various conditions/configurations. An initial attempt was made to compare the simulation with an experiment of Jet-A liquid atomizing in crossflowing air at ambient conditions,⁵⁷ where the experiment was set up to represent realistic fuel injector configurations and a comprehensive characterization of the inlet boundary conditions was not reported.⁵⁸ As found later,⁵⁹ a mismatch in liquid inlet velocity profile between the simulation and the experiment was related to a slight under-prediction of jet penetration. Also the spray distribution data for comparisons with simulations was available only at a downstream plane as limited by the measurement techniques.⁵⁸ A subsequent improved validation study⁶⁰ was conducted by simulating a detailed near-field experiment by Sallam *et al.*⁹ with well-characterized boundary conditions. In this paper, we present a more comprehensive validation including comparisons of near-field column features and droplet formation, and we validate the simulations at three Weber numbers, spanning breakup regimes ranging from bag, to multimode and shear breakup. More importantly, we also exploit the validated simulation results to explore the detailed atomization physics and scrutinize the aerodynamic impact on various atomizing flow features. Using the approach also followed by the experiment,⁹ we focus on aerodynamic effects that exclude other physical effects in spray formation such as gas/liquid inlet turbulence, liquid aeration, external excitation, complex injector geometry, cavitation, high-temperature high-pressure effects, and liquid evaporation.

In the following, the mathematical formulation and numerical implementation of the hybrid Eulerian-Lagrangian approach are briefly highlighted in Section II with more details documented in our previous work.^{53,54} In Section III, the presentation of results starts with a description of the computational setup. Quantitative near-field liquid atomization details extracted from the simulations are compared with experimental correlations.⁹ The comparison between uniformly refined grid simulations and Adaptive Mesh Refinement (AMR) simulations establishes the equivalence between the two configurations in capturing the surface instability and breakup. The detailed validation is then followed by a comprehensive discussion of the flow atomization physics based on

the uniformly refined grid simulations. This includes both liquid and gaseous flow physics as well as their interactions. Finally, summary and main conclusions from the work are provided in Section IV.

II. NUMERICAL METHODS

Since the numerical methods adopted in this paper have been comprehensively described in our previous work,^{53,54} only a brief highlight is provided here for the completeness of the paper.

In this work, it is assumed that the two-phase flow of liquid and gas is incompressible and can be represented by a single fluid formulation. Under these assumptions the governing conservation equations are

$$\nabla \cdot \mathbf{u} = 0, \quad (1)$$

$$\frac{\partial \mathbf{u}}{\partial t} + \mathbf{u} \cdot \nabla \mathbf{u} = \frac{1}{\rho} \nabla \cdot (-p\mathbf{I} + 2\mu\mathbf{D}) - \sigma\kappa\nabla H, \quad (2)$$

where p is the pressure, ρ the density, μ the viscosity, \mathbf{I} the identity tensor, \mathbf{D} the deviatoric strain rate tensor, σ the constant interfacial tension, κ the local curvature, and H the Heaviside function defined as

$$H(\Phi) = \begin{cases} 1 & \Phi \geq 0 \quad (\text{liquid}) \\ 0 & \Phi < 0 \quad (\text{gas}) \end{cases}. \quad (3)$$

Here Φ is a function that identifies the interface location. The density and viscosity are correspondingly defined as

$$\begin{aligned} \rho &= \rho_l H(\Phi) + \rho_g [1 - H(\Phi)], \\ \mu &= \mu_l H(\Phi) + \mu_g [1 - H(\Phi)]. \end{aligned} \quad (4)$$

The motion of interface follows

$$\frac{\partial \Phi}{\partial t} + \mathbf{u} \cdot \nabla \Phi = 0. \quad (5)$$

As noted, Sussman's CLSVOF method⁴² is used to directly capture the evolution of liquid-gas interface. Briefly, the Navier-Stokes equations are augmented with both a level set signed distance function ϕ and volume fraction function F to describe the time-evolving interface. Both ϕ and F obey Eq. (5). After advecting both scalars in time, the interface normals are determined from the level set function and used to reconstruct a surface for each grid cell partially filled with liquid as prescribed by the VOF distribution. This interface is then used to re-initialize a level set distance function ϕ . The method capitalizes on the advantages of both the accurate geometric interface representation in level set methods and the volume-preserving properties in volume of fluid methods.

Due to the drastic density/viscosity differences between liquid and gas phases, the velocity gradient is much larger in the gas phase than in the liquid phase. Conventional discretization of the momentum equation across the interface by a single fluid representation introduces large numerical errors due to poorly resolved velocity gradient on the gas side, which leads to flow divergence if special care^{49–52} is not taken. In our approach, the two-phase Navier-Stokes equations are solved using a two-fluid advection approach^{42,61} to avoid artificial smearing of velocity field across the interface. The interface is advected using a divergence free extrapolated liquid velocity field with no smearing error. On the other hand, a liquid-gas combined velocity is used in the velocity diffusion and pressure projection steps. The pressure projection equation is solved using a Multi-Grid Pre-conditioned Conjugate Gradient (MGPCG) method. The method is augmented by a ghost fluid (GF) treatment for pressure jump conditions to achieve stable and fast pressure solution. Such a suite of sharp interface treatments mitigates the problem of solver divergence that typically occurs at high density ratios.

The above Eulerian approaches are implemented under the framework of a block structured AMR.^{42,62} The complex breakup/coalescence of a liquid-gas interface during atomization can be

TABLE I. Properties (in SI units) of water used in the simulations.

ρ_l	μ_l	ρ_g	μ_g	r_ρ	r_μ	σ
997	0.000 894	1.18	0.000 018 6	845	48	0.0708

efficiently captured with the aid of AMR. However, the accurate simulation of the evolution of the multitude of very fine droplets that are generated after atomization still requires a high local grid density. In our previous work,^{53,57} a numerical approach has been developed to change the way the liquid phase is described in dilute regions from Eulerian level-set/volume-of-fluid representation to Lagrangian particle representation, similar to the algorithms implemented by Herrmann.⁵⁵ The transformation is allowed to occur when a number of criteria (e.g., size, sphericity, and diluteness criteria) are met.^{53,57} Previously, we have shown that our particular implementation of this Eulerian to Lagrangian droplet transformation,⁵⁷ when combined with the AMR technique, provides additional cost-saving benefits, especially when jet column and dense spray region occupy only a small part of the domain.

III. RESULTS

A. Physical parameters and computational setup

The simulations were configured based on the experiment by Sallam *et al.*⁹ to measure the near-field characteristics of non-turbulent water jet in cross flowing air ($r_\rho = 845$) at ambient conditions. The detailed material properties and conditions are listed in Tables I and II, respectively. The multiphase breakup is controlled by the competition between surface tension and aerodynamic flow forces at the liquid-gas interface. At high flow Reynolds numbers as in our study (see Table II), the effects of viscosity are secondary and the Weber number that represents the ratio of gas phase forces to surface tension plays a critical role in determining the mechanisms of breakup. The momentum flux ratio is fixed at $q = 88.2$, and three gas Weber numbers are selected, covering a range of breakup regimes,⁹ namely, $We = 10$ for bag breakup, $We = 40$ for multimode breakup, and $We = 160$ for shear breakup.

In the simulations, the coordinate system has the x -axis in the crossflow direction and the z -axis in the direction of liquid injection. The computational domain is a box of $3.0 \text{ cm} \times 2.0 \text{ cm} \times 5.0 \text{ cm}$. The jet orifice is located at a coordinate of $(0.2, 1.0, 0.0)$ with a diameter of $d_0 = 0.8 \text{ mm}$. Impermeable no-slip boundary conditions are imposed at the $z = 0$ plane, except at the jet orifice. Velocity inflow is imposed at the inlet boundary located at $x = 0 \text{ cm}$ and at the jet orifice. Outflow boundary conditions are imposed on the remaining boundary planes. The time stepping of the simulation is defined by two criteria: CFL criterion and surface tension criterion⁴² $\Delta t < \min\left(\frac{1}{2}\frac{\Delta x}{|u^x|}, \frac{1}{2}\sqrt{\frac{\rho_l}{8\pi\sigma}}\Delta x^{3/2}\right)$. Each simulation starts from the instant when the jet is injected into a uniform gaseous crossflow. The simulations reach full penetration within 4 ms, 2 ms, and 1 ms in physical time for the $We = 10, 40$, and 160 cases, respectively. These simulations are continued for another such period for each case for collecting statistics. An example of instantaneous snapshot when the liquid jet reaches full penetration for the $We = 40$ case is shown in Fig. 1.

TABLE II. Conditions (in SI units) employed in the simulations. The momentum flux ratio q is maintained constant while the Weber number We is increased from 10 to 160.

Cases	U_l	U_g	$q = \rho_l U_l^2 / \rho_g U_g^2$	$We = \rho_g U_g^2 d_0 / \sigma$	$Re_l = \rho_l U_l^2 d_0 / \mu_l$	$Re_g = \rho_g U_g^2 d_0 / \mu_g$
1	8.9	27.4	88.2	10	7 896	1391
2	17.7	54.8	88.2	40	15 791	2781
3	35.4	109.6	88.2	160	31 583	5562

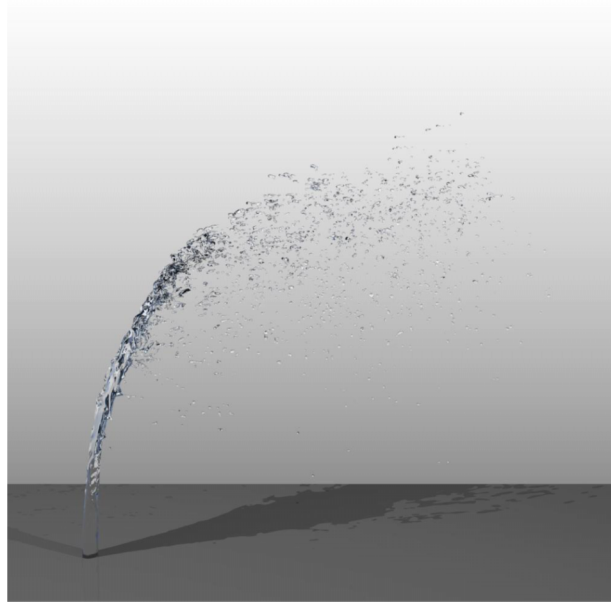


FIG. 1. Snapshot of a typical simulated liquid jet in crossflow, $We = 40$. The images of liquid surfaces in this and the following Figures 10 and 11 were generated using the ray-tracing technique that renders realistic three-dimensional perspectives under controlled lighting.

In the experimental study by Sallam *et al.*,⁹ the inlet flow turbulence is intentionally suppressed using a shock-tube and wind tunnel to generate uniform gas flow at high and low speed, respectively, and a sharp edge super-cavitating nozzle to achieve uniform liquid flow profile out of the injection orifice. As a result, the effects of inlet profile and turbulence on atomization were excluded and the work focused on liquid atomization due to aerodynamic forces. In our simulations, the exact configurations are emulated using plug-flow profiles for both the liquid and gas inlets. The thickness of the gas flow wall boundary layer at the injection orifice is estimated to be less than 20% of the injection diameter, and like in the experiment,⁹ the incoming gas flow is assumed to be uniform and the disturbance of the flow due to the presence of the wall boundary layer is neglected. Due to the presence of vena contraction^{63,64} in the experiment for the sharp-edge liquid nozzle, the measured jet diameter is smaller than the actual nozzle diameter. In our simulations, we exploit the availability of this measurement to avoid simulating the nozzle geometry and we simply set the inlet jet diameter to the measured value (0.8 mm for 1 mm nozzle). The distance for vena contraction (between the orifice and the end of jet contraction) was not reported in the experimental study⁹ and is usually small compared to the penetration length of the jet. In our simulations, this detail is neglected and the jets with 0.8 mm diameter start from the nozzle orifice location. The potential impact of crossflow on the liquid injection profile is assumed to be small and neglected at the relatively high momentum flow ratio ($q = 88.2$) in the current study. A test case of liquid jet penetrating into a long domain filled with quiescent gas phase in the absence of liquid inlet turbulence has also been simulated. In both the simulation and the experiment⁹ of such a straight jet without crossflow ($We = 0$), the absence of liquid inlet turbulence delays the development of surface waves on the jet column and the jet can penetrate long (longer than the domain height of 3 cm set for the crossflow cases) without triggering significant disturbances on its round surface. This indicates that the atomization physics to be presented here is controlled by the aerodynamic forces of the crossflow and the current experiment and simulation configurations eliminate the effects of liquid inlet turbulence in the study. Note that in the presence of liquid inlet turbulence, surface instabilities would start from the injector exit. For a straight turbulent liquid jet depending on the liquid momentum¹ or more precisely the liquid Reynolds number,⁶⁵ surface breakup may occur much earlier than what is witnessed here.⁶⁶ For a turbulent liquid jet in crossflow, surface instability develops earlier or even

starts at the injection orifice,⁶⁷ and the momentum-flux/velocity ratio may play a more important role in regulating the instability development.⁶⁸

The grid size is selected to be $\Delta x = 39 \mu\text{m}$ for all the simulations. With suppressed inlet turbulence, the smallest relevant flow scales are generated at the liquid-gas interface by multiphase flow instabilities. The grid resolution here is selected to be smaller than the smallest observable multiphase lengthscale, i.e., the ligament or droplet size, as measured in the experiment.⁹ Note that the actual pinch-off occurs at spatial and temporal scales that are infinitesimally small, much smaller than the smallest turbulent dissipation scale and approaching singularity in the continuum formulation.^{11,69} At these scales the continuum assumption breaks down and molecular scale physics starts to play a dominant role.¹¹ Approaching such scales using a continuum based method is beyond current and near-future computational capabilities. Moreover, proper simulation of the physics at these scales will require coupling with non-continuum models.⁶⁹ Here, we treat this impasse by postulating that the small scale physics has little impact on the large scale flow as long as all the scales witnessed in the experiment are resolved. This effectively guarantees that the liquid volume error is small since the experiments show increasingly diminished droplet number densities at the smallest sizes measured. In addition, as pointed out by Herrmann,⁵ from a numerical perspective the volume error induced by numerical topological change is on the order of grid size, and has negligible impact on large-scale features. The detailed validation results in Sec. III B verify the assumption made here and clearly indicate that for the flow considered here, the details of pinch-off physics do not have a significant impact on the atomization features of interest at the measurement scales.

In this work, three different grid configurations are first tested and compared for the $\text{We} = 40$ case, as demonstrated in Fig. 2. Uniform grid simulations (to be referred as UG in subsequent sections) which have the finest grids spread over the whole domain provide the most accurate solution by resolving both the liquid atomization processes and the gas flow using fine grids. The simulations were performed using over 5000 cores on the TITAN supercomputer of the Oak Ridge Leadership Computing Facility (OLCF) at Oak Ridge National Laboratory. Simulations that coarsen the gas phase solution using Adaptive Mesh Refinement (to be referred as AMR) and those that employ additional coarsening via the introduction of Lagrangian droplets (to be referred as AMR-DRP) were also performed using 24 cores each. It is observed in Table III that, indeed, AMR and droplet transformation significantly reduce the grid-count and simulation cost. It is important to note that the 15.7 days UG computation using 5008 cores translates to at least 9 years if using 24 cores

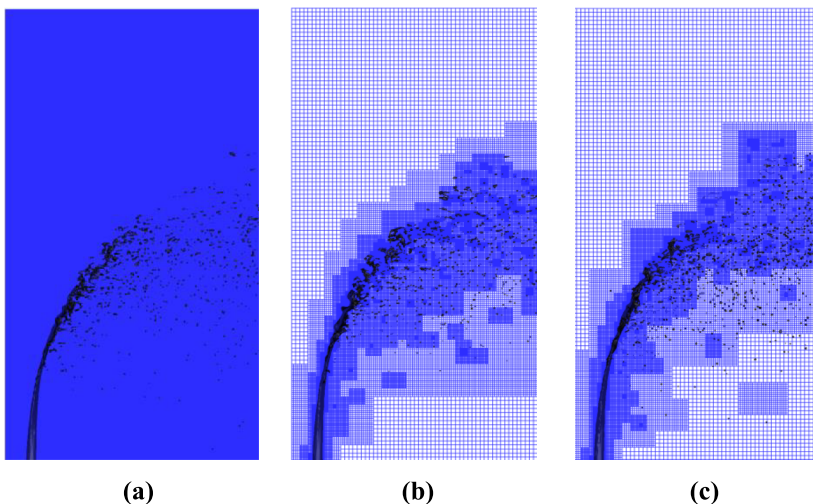


FIG. 2. Illustration of three grid configurations for the simulations: (a) Uniform Grid (UG) (simulated for all three We), having the finest grids spread over the whole domain, (b) AMR (simulated for $\text{We} = 40$), coarsening the gas phase solution using adaptive mesh, and (c) AMR+droplets (AMR-DRP simulated for $\text{We} = 40$), employing additional coarsening via the introduction of Lagrangian droplets.

TABLE III. Grid count and cost for three simulation configurations. Note that the grid-count reduction due to droplet transformation is small (5.5M for AMR-DRP vs. 7.1M for AMR), which is due to the compact simulation domain that is used to minimize the grid-count for the UG simulation. For cases with much larger domain with more droplets transformed to Lagrangian phase, the AMR-DRP simulation would show more cost advantage.

Simulation type	UG	AMR (3 level)	AMR-DRP (3 level)
Baseline grid	$768 \cdot 512 \cdot 1280$	$64 \cdot 48 \cdot 112$	$64 \cdot 48 \cdot 112$
Total grid count	503.3M	7.1M (steady-state)	5.5M (steady-state)
Cost of 10^4 steps	15.7 days (5008 cores)	20.8 days (24 cores)	14.7 days (24 cores)

assuming no memory limit for the machine. However, because the UG simulations provide the most reliable data for detailed validation and exploration of physics in both liquid and gas phase, the high cost UG simulations were performed for all three Weber numbers. They also establish the baseline to evaluate the accuracy of other grid configurations.

It can be expected that the 503×10^6 grid UG simulations not only require high computational power, but also pose significant challenges in storing and processing the large set of simulation data. Storing the three dimensional volume data for all the variables at different sampling instants may not be feasible on any state-of-the-art high performance storage systems. Loading and further analyzing the 3D volume data also require an extremely large effort. In this work, to manage the data within the storage and processing limit, the data are extracted only at two-dimensional surfaces of interest, stored, and later loaded for visualization and analysis. Special x, y, z planes and the liquid-gas interface are selected as the surfaces of interest for data reduction. All the vector components of the flow fields at all the surfaces of interest are stored at only one particular time instant to provide a complete instantaneous picture of the flow fields. The magnitude of these vector fields at a reduced number of surfaces is stored at a large number of time samples to help analyze the flow behavior in the temporal domain and obtain statistical information.

B. Quantitative column near-field validation

1. Column of liquid jet

In this section, several jet column quantities measured in the experiment are extracted from the simulation data and a detailed comparison between simulation and experiment is performed. The extraction of these quantities from the simulation data has been carried out in such a way as to emulate the experimental measurement approaches as much as possible. The quantitative comparisons for all the cases are summarized in Fig. 3.

Figure 3(a) compares the surface wavelength predicted by simulations and measured in experiments. The presence of travelling waves is identified using a Proper Orthogonal Decomposition (POD) based approach that was developed to analyze the dynamics of liquid jets.⁶ The POD results for all three cases are shown in Fig. 4. By analyzing a time series of images (such as those in the first column in Fig. 4), we are able to extract the first two most energy-containing POD modes that have the same frequency but 90° difference in phase, which indicates the presence of a travelling wave. For $We = 10$ and $We = 40$, the two modes shown in the second and third column of Fig. 4 clearly illustrate such wave structures and the wavelength seems to be smaller at larger We . For the case of $We = 160$, the traveling wave becomes more complex and three dimensional as shown in Figs. 4(g)-4(i). The wavelength can be quantitatively extracted by dividing the length of a wave-containing segment in the POD plots by the number of waves within the segment. The data in Fig. 3(a) show that the simulations at $We = 40$ and $We = 10$ predict very well the wavelengths on the column, and the data are in agreement with the experimental correlation⁹

$$\lambda_s/d_0 = 3.4We^{-0.45}. \quad (6)$$

Although the wave structures are observed to be more populated for the $We = 160$ case, the complex three dimensional wave patterns make it challenging to compute a simple wavelength from the POD results in Figs. 4(h) and 4(i).

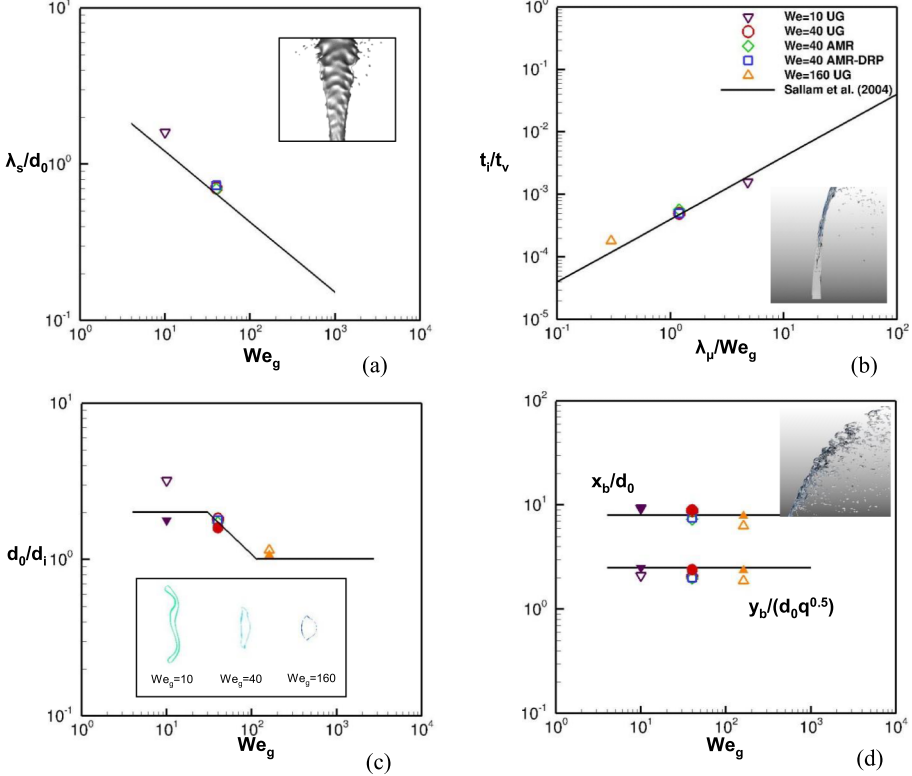


FIG. 3. Quantitative comparison of simulated liquid column data with experimentally calibrated correlations by Sallam *et al.*⁹ (a) surface wavelength, (b) location at onset of breakup, (c) deformation at onset of breakup, and (d) column breakup location. The mean values are extracted from the simulation data and plotted in comparison with correlations. The time periods for averaging are 4, 2, and 1 ms for $We = 10, 40$, and 160 , respectively. The simulation snapshots in the inset are used to explain the approaches for extracting properties from the simulation data.

Figures 3(b) and 3(c) compare the location for the onset of liquid breakup, and the column deformation in crossflow direction at this onset location. The location is identified as the location of first ligament that pinches off to form droplets. The deformation is obtained by computing the distance between the windward and the leeward surface in a plane cut through the onset location (see Fig. 3(c) inset). These quantities computed at 100 sample instants are averaged to provide the data points shown in Figs. 3(b) and 3(c). It is observed that the onset location and column deformation at $We = 40$ compare well with experimental correlations,⁹

$$t_i/t_v = 0.0004 (r_\mu/We), \quad (7)$$

$$d_0/d_i = \begin{cases} 2 & 4 < We < 30 \\ 12We^{-0.53} & 30 \leq We \leq 110 \\ 1 & We > 110 \end{cases}, \quad (8)$$

where $t_i = z_i/U_l$, $t_v = \rho l d_0^2/\mu_l$, and $r_\mu = \mu_l/\mu_g$. The comparison is good for the $We = 160$ case as well, while discrepancy is observed for the $We = 10$ case in comparing the deformation. The XY-plane cut of the jet columns at the stripping onset location shown in the inset of Fig. 3(c) demonstrates that d_i increases with increasing We , based on d_i being defined as the minimum column width in the crossflow direction. However, using only the XZ side-view (approach used in Ref. 9) d_i can be overestimated because of the obscuration introduced by the protruding ligaments as shown in the inset for the $We = 10$ case. This explains the smaller d_i (larger d_0/d_i) extracted from the simulation data compared to the measured values in Ref. 9. In fact, the data extracted using

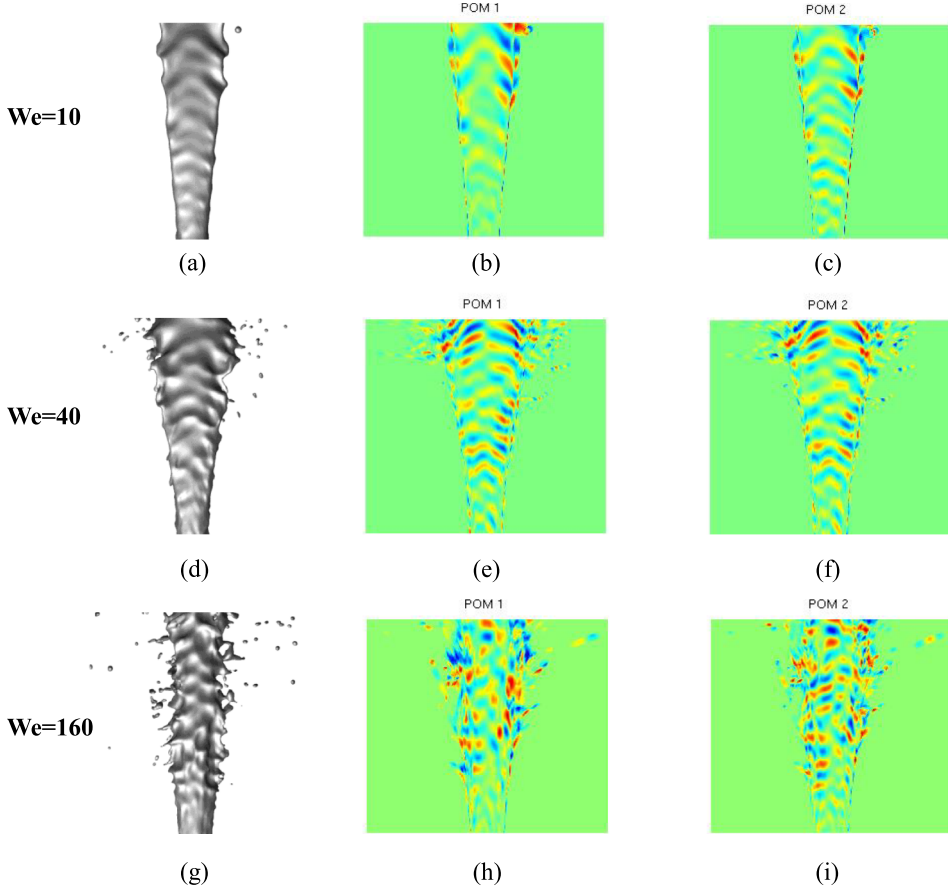


FIG. 4. Comparison of liquid column waves at different Weber numbers (1st column). The presence of travelling waves is identified using a Proper Orthogonal Decomposition (POD) based approach. The first two most energy-containing POD modes, having the same frequency but 90° difference in phase, were extracted (2nd and 3rd column). The wavelength was computed by dividing the length of a wave-containing segment in the POD plots by the number of waves within the segment.

only the XZ side-view simulation images (shown by the solid symbols) compare better with the experimental correlation.

In Fig. 3(d), the locations for the breakup of liquid column are compared. The breakup locations are identified as the locations of column liquid no longer being contiguous from the injection point. The locations computed at 100 sample instants are averaged to provide the data points shown in Fig. 3(d). The experimentally measured column breakup locations were fitted onto the following correlations⁹ and these are also shown in Fig. 3(d):

$$x_b/d_0 = 8.0, \quad (9)$$

$$z_b/(d_0 q^{0.5}) = 2.5. \quad (10)$$

Overall, the breakup location z_b identified from the simulation data matches experimental correlations (9) and (10), being slightly smaller for most cases. The other minor difference is that as Weber number increases, both breakup locations x_b and z_b obtained from the simulation data shift towards the injection orifice instead of being a constant as prescribed by correlations (9) and (10). Note that two different views (XZ view and YZ view) are used to help identify the breakup location. If only XZ side-view images are used, as has been the practice in the experiments,^{1,9} the breakup location may be over-estimated due to the obscuration imposed by neighboring liquid structures. The breakup locations identified using only the XZ side-view simulation images (as shown in Fig. 3(d) by solid symbols) tend to shift to slightly larger values, better matching the correlations, although still showing a trend of decrease with increasing We.

TABLE IV. Standard deviations for simulation data of case 2 ($We = 40$) in Fig. 3.

Simulation type	UG (%)	AMR (%)	AMR-DRP (%)
λ_s/d_0	11.2	15.6	13.2
t_i/t_v	10.8	11.0	9.6
d_0/d_i	9.1	6.9	7.1
x_b/d_0	12.0	9.4	9.2

The predictions of small-scale column features for the simulations using different grid configurations (UG, AMR, AMP-DRP) for the case of $We = 40$ are compared in Fig. 3 as well. The standard deviations of the data for these cases are listed in Table IV. The zone enclosing the jet column is resolved to the same level of accuracy in all grids using either uniformly or locally refined mesh. Therefore, as shown in Fig. 3(d), the jet breakup location or the penetration length predicted using different grid configurations match quantitatively. The surface wavelength, jet deformation, and stripping location are also well predicted using AMR (Figs. 3(a)-3(c)) due to the same fact that the liquid structures resulting from interfacial instabilities and breakup are well captured by the fine mesh near the interface. The AMR-DRP case also compares well with the AMR case for all the column features because the same refinement is applied near the jet column. As shown in Table IV, the standard deviations of the data are very close for all three configurations, and they are mostly around 10%, consistent with the 10% uncertainty for most correlations reported in the experimental study.⁹ The slightly higher deviations in surface wavelength for AMR and AMR-DRP cases can be attributed to the numerical error in the gas phase solutions.

The instantaneous liquid jet and the corresponding color contour of velocity components for the $We = 40$ case are compared in Fig. 5. Compared to the UG case, the AMR case has reduced resolution in the gas dominated regions. The large scale flows such as the negative U-velocity zone (Fig. 5(a) vs. Fig. 5(b)) and the positive W-velocity zone (Fig. 5(g) vs. Fig. 5(h)) behind the liquid column are captured in the AMR simulation while the small scale flow fluctuations are suppressed by numerical dissipation using locally coarsened grid. However, the coarsely resolved gas flow downstream does not affect the overall deflection and penetration of the jet column. The AMR-DRP case also compares well with the AMR case in terms of flow field, jet column deflection, and penetration. Additional numerical dispersion error is introduced in the gas flow due to the use of Lagrangian droplet models that couple with the flow solver. As a result, the droplets are dispersed even more in the downstream region (Fig. 5(b) vs. Fig. 5(c)). In summary, using the UG, AMR, and AMR-DRP configurations, the near-field column details of the jet under current conditions can be quantitatively captured by the simulations to a similar degree of accuracy, irrespective of the differences shown in the gaseous flow predictions.

2. Formation of droplets from liquid column

Sallam *et al.*⁹ also reported the measurements of the size and velocity of the droplets initially formed off the jet column, even though these droplets (some of them are still large) may experience further secondary breakup downstream. Similar procedures were taken here in the simulation study by capturing the liquid blobs initially formed from the elongated ligaments on the column. Instead of being captured using post-processed 2D snapshot images as in the experimental study,⁹ they were systematically captured in real time by leveraging the Lagrangian transformation algorithms introduced in our previous work.^{53,54} Since the near-field column details have been shown in Sec. III B 1 to not be sensitive to grid configurations, all three Weber number cases using the AMR-DRP configuration were re-simulated with a modified set of droplet transformation criteria: the size and diluteness criteria are not imposed while the sphericity criterion remains active to avoid erroneous transformation of elongated ligaments. Since comparisons are to be made regarding the droplets formed off the column, possible secondary breakup of these droplets was not considered in the simulations. Droplet data including sizes, locations, and velocities at the instant of transformation

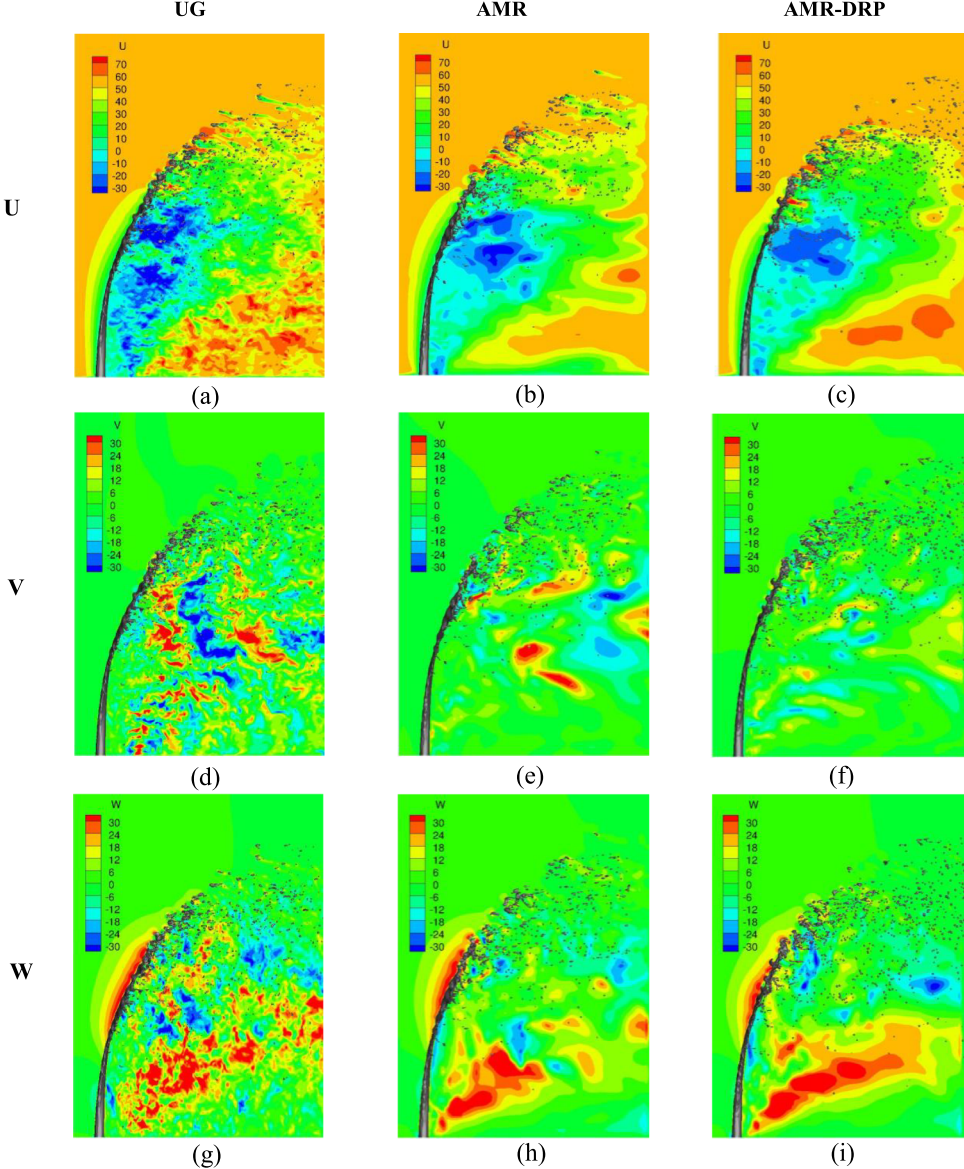


FIG. 5. Comparison of flow velocities at the mid-plane ($y = 1 \text{ cm}$) using different grid configurations as in Fig. 2, $We = 40$.

were sampled for a long period after the jet reaches full penetration stationary state. Over 20 000 droplets were collected for each case. The size and velocity of such collected droplets for the $We = 40$ case are shown in Figs. 6(a) and 6(b), respectively.

The size distributions of droplets formed off the jet column are shown in Fig. 7. To check the sensitivity of droplet size to the change of We , the data obtained at different We are shown in three columns. The data for the $We = 160$ case are compared with experimentally obtained correlation for shear breakup regime only,⁹

$$d_p/d_0 = \begin{cases} 4.32[(\nu_l z) / (U_l d_0^2)]^{0.5} & (\nu_l z) / (U_l d_0^2) < 0.001 \\ 0.132 & (\nu_l z) / (U_l d_0^2) \geq 0.001 \end{cases}, \quad (11)$$

where d_p is the droplet diameter and $\nu_l = \mu_l / \rho_l$. The correlation curves fall within the data collected as shown in Fig. 7(c). The number mean sizes for each location (denoted by the solid “square” symbols) are close to the correlation for the $We = 160$ case, although the simulation data do not

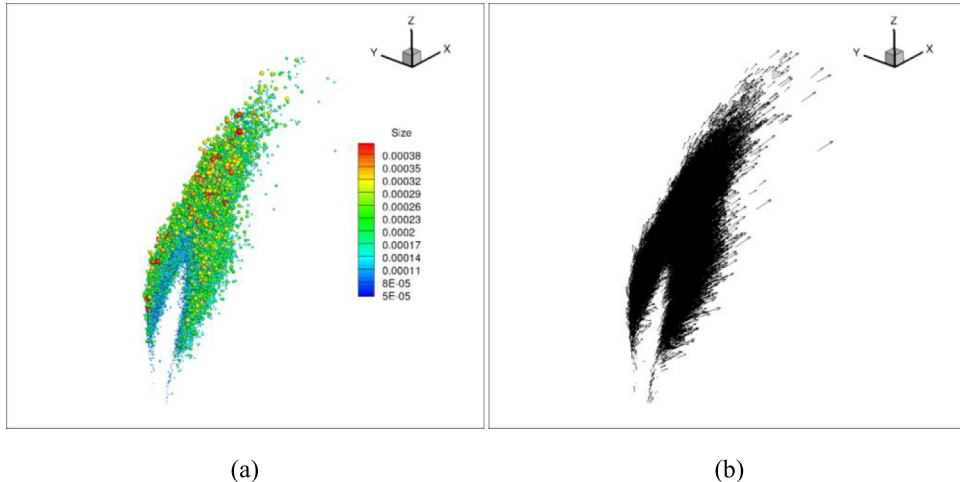


FIG. 6. (a) Size (color map) and (b) velocity (vector) of liquid blobs initially formed from the elongated ligaments on the column were collected for over 20 000 droplets. These quantities were systematically captured in real time using modified Lagrangian transformation algorithms. The $We = 40$ case is shown in this figure as an example.

seem to show saturation in droplet size as z/d_0 increases. While the We dependence of the droplet size distribution was not experimentally investigated, it is reflected in the simulation data. Very few droplets are formed at the lower part of the column for the case of $We = 10$ due to the delayed onset of surface breakup as shown in Fig. 3(b). Slightly more droplets are generated at the lower part of the column for the case of $We = 160$ (Fig. 7(c)) than $We = 40$ (Fig. 7(b)). The detailed size probability distribution (number density) at three different z locations is shown in the bar-chart (d)-(l). The sizes with the highest probability are mostly around 100–120 μm at all locations for all We . For the case of $We = 10$, the largest droplet size observed increases from 240 μm to more than 400 μm from $z/d_0 = 15$ to $z/d_0 = 25$ due to the breakup transition from stripping to the rupture of thick ligaments enclosing the “bag,” as will be explained next. The sizes of the droplets resulting from the breakup of those thick ligaments are large while their number density is small. As We increases from 10 to 40, larger size droplets appear at $z/d_0 = 15$ due to the earlier onset of surface stripping for $We = 40$. The size distributions for $We = 40$ and $We = 160$ cases are similar except an earlier depletion of liquid and less number of droplets for sampling at $We = 160$ (Figs. 7(c) and 7(l)).

The distributions of the three velocity components of the droplets formed near the liquid surface are plotted in Fig. 8. The data obtained for different We are shown in three columns. As in Ref. 9, the droplet x velocity component is scaled by the combination of cross flow gas velocity and density ratio,

$$u_p/\hat{u}_l = u_p(\rho_l/\rho_g)^{0.5}/U_g, \quad (12)$$

to reflect the scaling of momentum exchange between liquid and gas. The y and z velocity components are scaled by the liquid injection velocity U_l . Experimental correlations for the shear-breakup regime were obtained for the U and W velocity components,⁹

$$u_p/\hat{u}_l = 6.7, \quad (13)$$

$$w_p/U_l = 0.7, \quad (14)$$

because only the 2D side-view images were used in the analysis. The correlation curves fall within the data collected as shown in Fig. 8. The mean velocities for each location (denoted by the solid “square” symbols) are close to the correlation for the $We = 160$ case, with a slight over-prediction of U velocity component and under-prediction of W velocity component. The mean velocities for the $We = 40$ case are also close to the correlation and for the $We = 160$ case larger deviation is observed. The oscillations in the mean values at smaller z/d_0 are due to the small number of samples available as shown by the scattering of data. For all three cases, an increase in U with increasing z/d_0

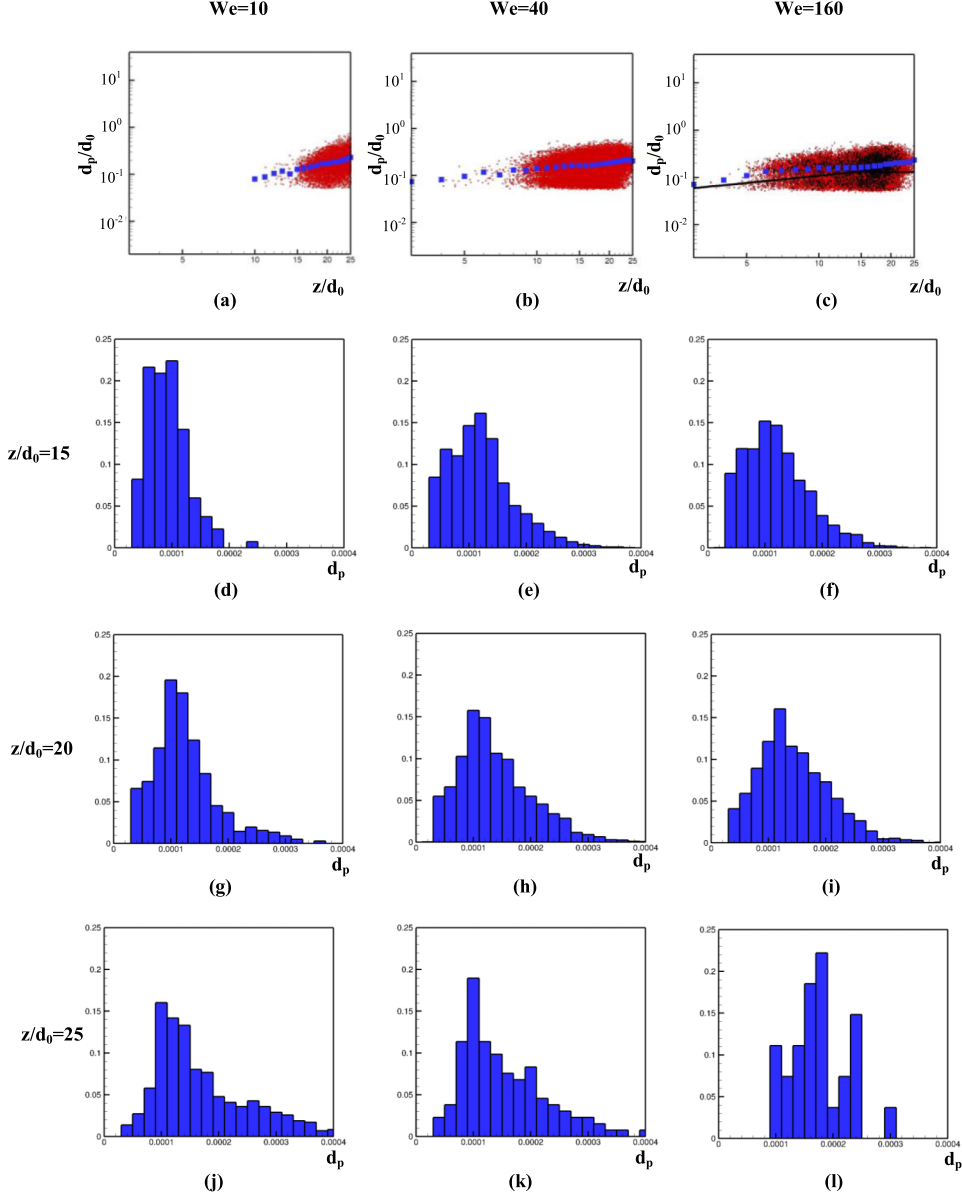


FIG. 7. (a)-(c) show droplet size along z coordinates at different We . The mean values for each z coordinate are shown by the blue symbols. Experimental correlation (solid line) for shear breakup is also shown. (d)-(l) show the corresponding droplet size probability distribution at different z locations. The probability is represented by the droplet number density. The unit for d_p is “meter.”

is not reflected in the constant-value correlation. The trend may be explained by the acceleration of liquid element along the jet column by the gas flow in the x -direction. In the inset of Figs. 8(a)-8(c), the size-conditioned mean velocities are also plotted for different size bins. For all three cases, the size-conditioned mean velocities are quite similar. The size-conditioned U velocity decreases overall with increasing size probably due to the slower acceleration of the larger droplets (higher Stokes number) in the crossflow direction. The size conditioned W velocity increases overall with increasing size probably due to the slower deceleration of the larger droplets in the upward injection direction. The non-monotonic trend shown for smaller droplet sizes can probably be attributed to spatial distribution effect. Specifically, the concentration of smaller droplets may be larger closer to the column due to stripping and these droplets have smaller U velocity and larger W velocity

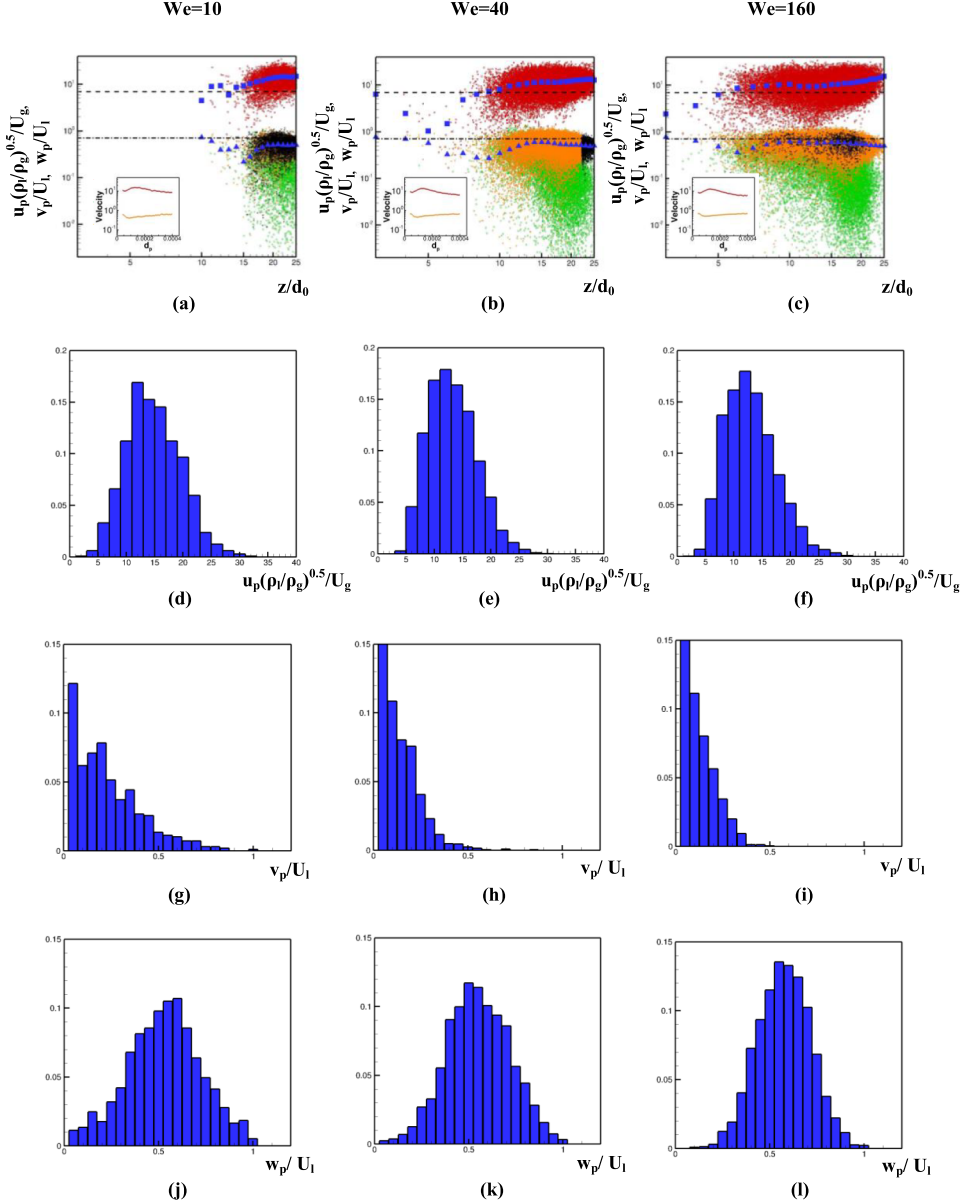


FIG. 8. (a)-(c) show droplet velocities along z coordinates at different We . The u -velocity is denoted by “red” dots, the v -velocity is denoted by “green” dots, and the w -velocity is denoted by “orange” dots. The mean values of u and w velocities for each z coordinate bin are shown by the blue symbols. Experimental correlations for u (dashed line) and w (dashed-dotted line) velocity components are also shown. The inset of (a)-(c) shows the size conditioned mean of velocities at different size bins with bin size of $10 \mu\text{m}$. The mean u -velocity is denoted by “red” curve and the mean w -velocity is denoted by “orange” curve. (d)-(l) show the corresponding droplet velocity probability distribution at $z/d_0 = 20$.

(see (a)-(c) main figure). The detailed velocity probability distributions at $z/d_0 = 20$ are shown in the bar-charts (d)-(l). The distributions for the U component are similar for all three conditions, indicating that the droplet velocity overall scales with the gas velocity in the cross flow direction. The peak value for the U velocity component ~ 12 is consistent with the mean values in plot (a)-(c), larger than the value of 6.7 in the correlation. The peak values for the W velocity component in the range of 0.5–0.6 are in reasonable agreement with the value of 0.7 in the correlation. The larger maximum values in the V component and higher probability of small W component for the case of $We = 10$ are probably due to the formation of wider jet column (as will be explained next) and

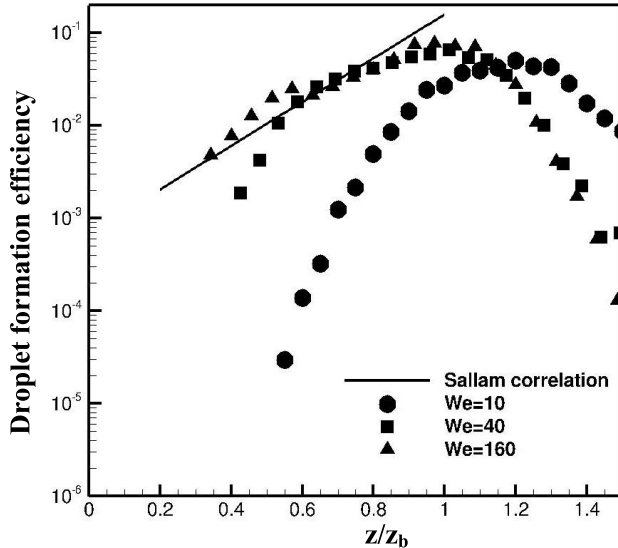


FIG. 9. Efficiency of droplet formation along the z direction for different We . The quantity represents the flux of liquid through a downstream column projected area scaled by the flux of a contiguous liquid ligament of density ρ_l moving away from the column at velocity u_p . In the postprocessing of simulation data, the droplet flux is computed along the column by dividing the surface into different bins along the z direction.

therefore the increased V component and decreased W component when they are formed at the column edge. The distributions for the V component show a peak around 0, indicating a very small transverse motion for most droplets when they are initially formed.

In addition to droplet size and velocity, droplet formation rate is another quantity extracted from the experimental data.⁹ The quantity represents the flux of the liquid leaving the contiguous jet column and becoming discrete droplets. In Ref. 9, a quantity called droplet formation efficiency is defined as

$$\varepsilon = \dot{m}'' / (\rho_l u_p), \quad (15)$$

where \dot{m}'' is the droplet formation rate, representing the flux of liquid through a downstream column projected area. $\varepsilon = 1$ represents the case of a contiguous liquid ligament of density ρ_l moving away from the column at velocity u_p . In our simulation study, the flux \dot{m}'' is computed as

$$\dot{m}''(i) = \frac{\pi \rho_l \sum_{j=1}^{N_i} (d_p^j)^3}{6\Delta t_{sample} A_i}. \quad (16)$$

The droplets generated along the column surface are lumped into different bins along the z direction. The bin size is selected to be d_0 . The column projected area A_i is constant d_0^2 for all the bins. The summation in Eq. (16) is over all the droplets formed within the i th bin. Therefore, the efficiency is computed as

$$\varepsilon = \frac{N_i \pi \sum_{j=1}^{N_i} (d_p^j)^3}{6\Delta t_{sample} A_i \sum_{j=1}^{N_i} u_p}. \quad (17)$$

Fig. 9 shows the computed efficiency along z locations at different We . At all three conditions, the efficiency first increases with increasing z due to the increased frequency of ligament formation along the column. It then decreases beyond the column breakup point $z/z_b = 1$ due to the depletion of liquid, where z_b (taken as $2.5(d_0 q^{0.5})$ in Eq. (10), constant for all three cases) is the column breakup location in the z direction. The starting location with finite droplet formation rate is consistent with location for the onset of surface breakup (see, e.g., Fig. 3(b)), which increases with decreasing We . Compared with the case of $We = 40$ and $We = 160$, the case of $We = 10$ has lower efficiency at the lower part of the jet and slightly higher efficiency at the upper part.

As will be explained next, it is mostly due to much less droplet stripping at the lower part and strong bag breakup with formation of long ligaments at large z locations. The cases of $We = 40$ and $We = 160$ have very similar breakup efficiency. The $We = 160$ case seems to match better with the experimental correlation (solid line in Fig. 9)⁹

$$\varepsilon = 6.89 \times 10^{-4} \exp(5.43z/z_b), \quad (18)$$

which was developed for the jets in shear breakup regime only. At the lower part, the efficiency is slightly higher for the $We = 160$ case than for the $We = 40$ case, due to an earlier onset of stripping (Fig. 3(b)) and a higher stripping rate at $We = 160$.

This ends a comprehensive validation of the simulation approach against the experiment. Next the detailed simulation data will be used for an in-depth exploration of the physics of liquid jet atomization, gas flow, and their interactions.

C. Physics discussion

1. Liquid jet atomization

In Fig. 10, several common features of atomization previously reported^{1,3,4,9,12,14,15} are clearly illustrated with jets shown in three different views. The side-view images in Figs. 10(a)–10(c) qualitatively compare well with those in the experimental report (Fig. 1 in Ref. 9) while Figs. 10(d)–10(f) and 10(g)–10(i) provide two additional views that were not accessible in the experimental study. These additional views not only provide more accurate ways of quantifying the process (as shown in the previous validation section) but also help better illustrate the three-dimensional liquid structures and shed light on the underlying physics.

Commonly for all three cases at different We , as the jet penetrates into the crossflow, it bends towards the flow direction. Due to the jet blockage, the gaseous flow changes direction to pass around the liquid jet. The pressure difference generated by the liquid blockage leads to the deformation and transverse widening of the liquid jet column (Figs. 10(d) and 10(e)). Due to the liquid-gas aerodynamic interaction, surface waves are formed on the windward side of the column and the waves propagate and grow along the jet column. A notable feature of these waves observed from the front-view (Figs. 10(d), 10(e), 4(a), and 4(d)) is their “ Λ ” shape. This is because the transverse widening of the jet leads to an additional traveling velocity component in the transverse directions for the surface waves. The combination of upward and transverse velocity components leads to local wave traveling velocities in separate “up-left” and “up-right” directions and the formation of “ Λ ” shape waves. On the edge of the column, these waves lead to local surface perturbations. Due to the high local gas shear (Figs. 10(a)–10(c) inset) these perturbations are further amplified and ligaments and small droplets are stripped off the column. Finally, the windward surface waves are amplified along the column, and become three-dimensional probably due to a secondary instability and sufficiently strong to fragment the jet column into ligaments/large drops that further break up into smaller droplets (Figs. 10(g)–10(i)). Droplets of different sizes generated along the jet column continue to be transported and interact with the gas flow downstream. It is worth noting that in several experimental studies,^{1,70} the oscillations observed at the liquid surfaces (surface waves) were identified as windward waves and leeward waves based on only the side-view black and white images. This notion of two different waves may be misleading because as shown in the zoomed view of jet breakup in the inset of Figs. 10(a)–10(c), the oscillations of the surfaces on the leeward side observed from the side-view (a)–(c) mostly appear as the ligaments/droplets formed due to the surface instability and stripping occurring at the transverse edge of the jet column, as also shown from other views in (d)–(i). The experimentally observed leeward oscillations should not be interpreted as wave formation on the leeward column surface.

The qualitative features of liquid jet deformation and breakup at different We are compared in both the instantaneous snapshots of liquid surfaces in Fig. 10 and averaged pictures in Fig. 11. Due to the same momentum ratio $q = 88.2$ for all three cases, before the instability and breakup of liquid surface set in, the initial momentum exchange between liquid and gas follows a similar pattern, independent of We . Therefore the initial jet deformations close to the jet orifice are quite similar. In

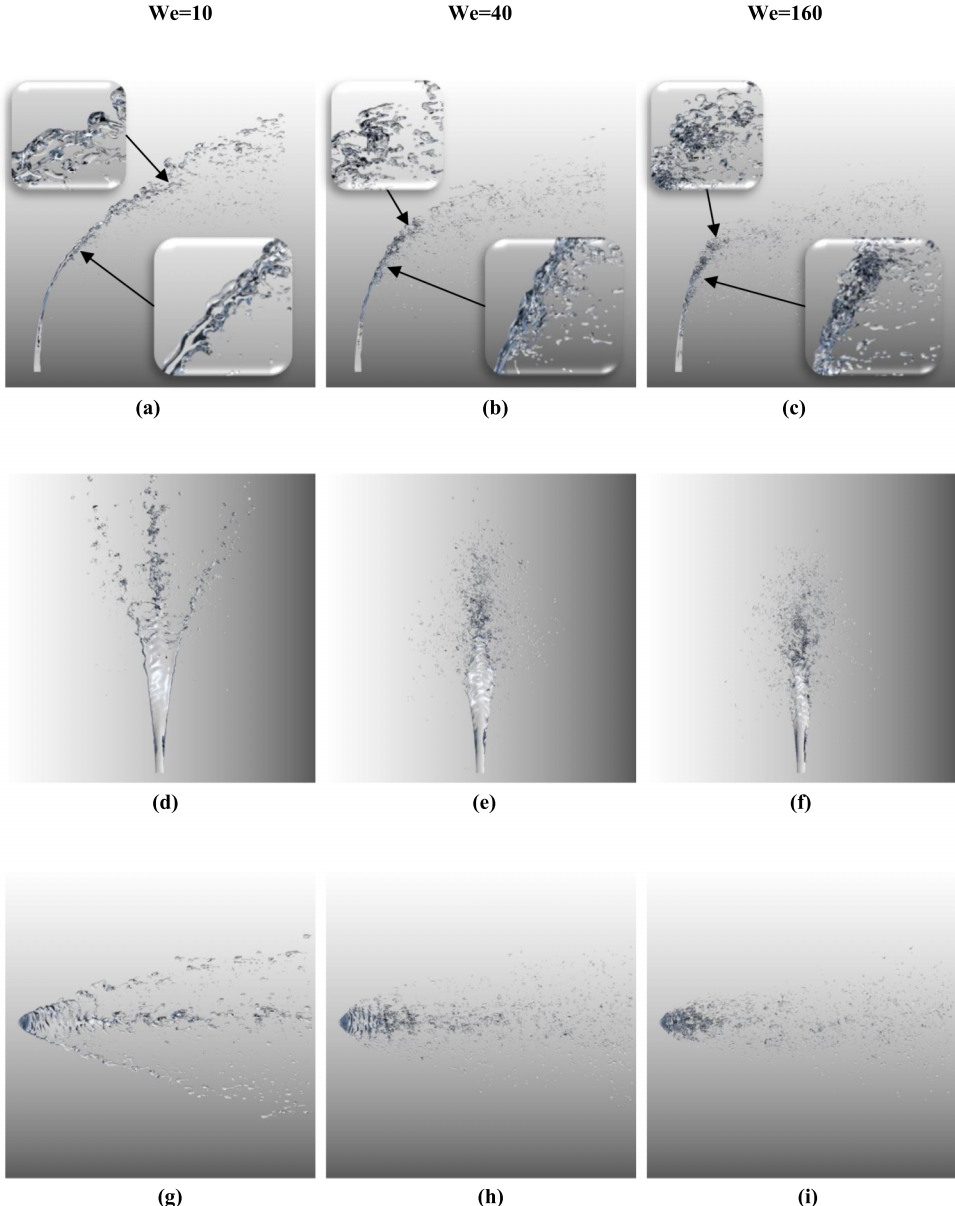


FIG. 10. Comparison of instantaneous liquid surfaces in three views at different We . Insets of (a)-(c) show zoomed views of the details for column breakup from the column end (upper left inset) and surface stripping from column surface (lower right inset). The side-view images (a)-(c) qualitatively compare well with those in the experimental report, while images (d)-(f), (g)-(i) provide two additional views that were not accessible in the experimental study.

Figs. 11(a)–11(e), the averaged column surface boundaries for the $We = 160$ case (denoted by the black curve) are plotted on top of the averaged liquid surfaces for all three cases. Since the averaged gray-scale images (Figs. 11(c) and 11(e)) are blurred at column surfaces, such column boundaries are identified using an edge-detection software to find the pixels that have $\geq 2^\circ$ magnitude difference (on a 0-255 scale) than their neighboring pixels. The column trajectory based on Sallam's experimental correlation in shear breakup regime⁹ is also plotted in Fig. 11(c) to compare with the averaged column boundary extracted for the $We = 160$ case. It is noted that the correlation is calibrated by curve-fitting the data for the whole spray (column plus droplet region) and its accuracy in the column region alone plotted in Fig. 11(c) is not well established. Despite this reasonably good agreement is witnessed, demonstrating the effectiveness of the simulation in capturing the column

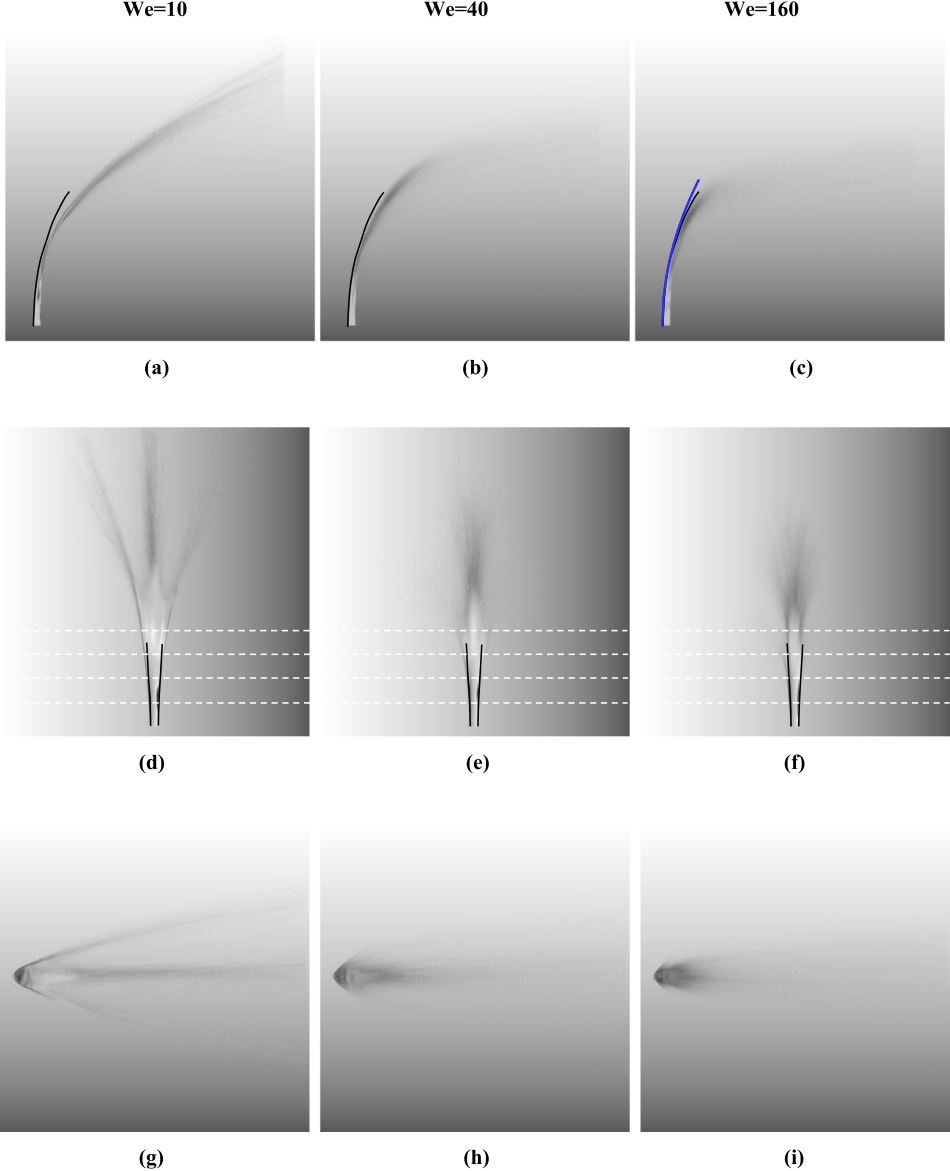


FIG. 11. Comparison of averaged liquid surfaces in three views at different We . The time periods for averaging are 4 ms for $We = 10$, 2 ms for $We = 40$, and 1 ms for $We = 160$. The averaged column surface boundary for the $We = 160$ case (denoted by the black curve) is plotted on top of all three cases in (a)-(c) and (d)-(f) to demonstrate the differences in column deflection in crossflow direction and width in the transverse direction. The column trajectories based on experimentally obtained correlations for shear breakup regimes are also plotted for the $We = 160$ case in (c). The white dashed lines in (d)-(f) indicate the locations of planes to be shown next in Fig. 12.

deflection. For different We , the similarity in column deformation is observed in the lower part of the jet close to the injection orifice. More detailed column deformation and nearby velocity field at different z -planes are shown in Fig. 12. At the plane close to the injection orifice ($z = 0.25$ cm), the deformed 2D cross-section shapes (white curves) of the column are quite similar. The color contours are scaled proportionally to the gas inflow velocities in Fig. 12. The comparison in (a)–(c) depicts very similar large scale flow structures as well.

The gas Weber number plays a critical role in controlling the surface instability and breakup. Evidence of this can be seen in Fig. 3(a) where the surface wavelength decreases with increasing We . Substantial research effort has been expended^{6,7,9,70,71} towards understanding the physical

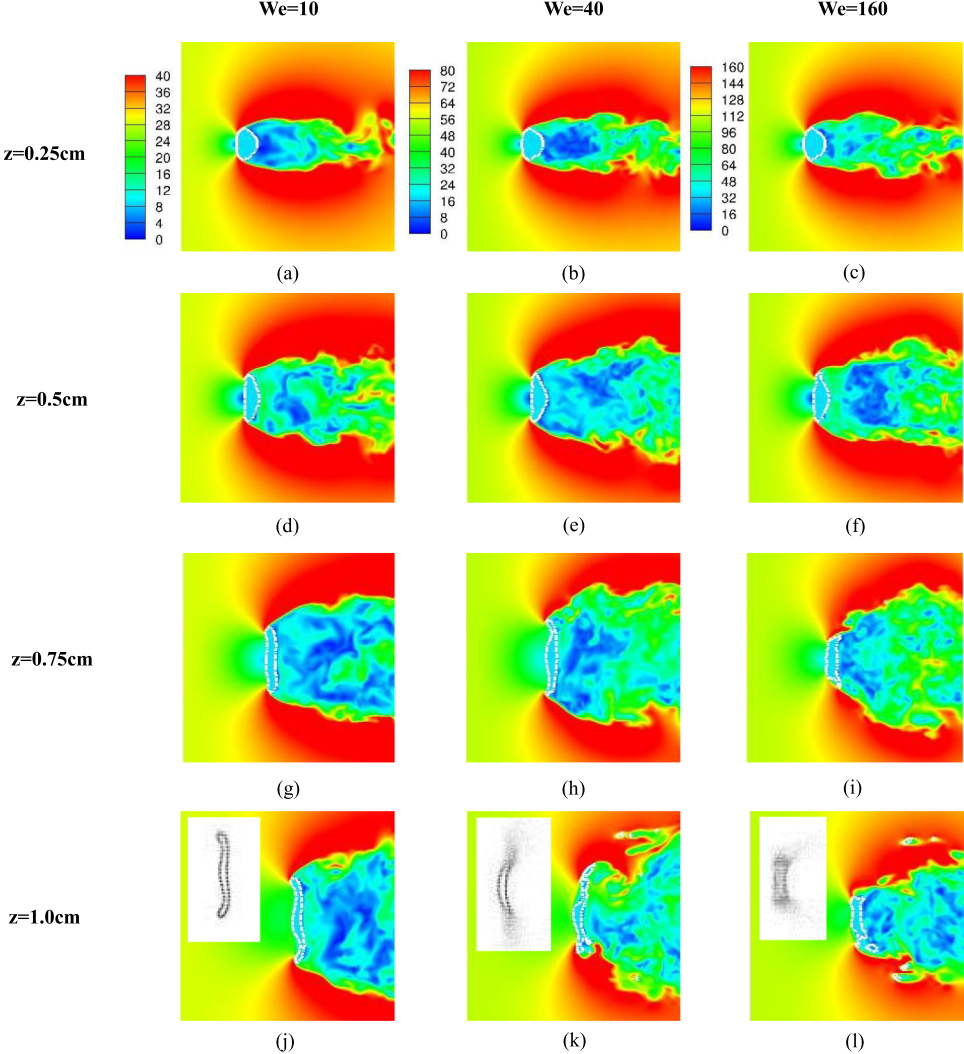


FIG. 12. The instantaneous jet column shapes (white lines) together with velocity magnitude contours at different z -planes close to the jet orifice (shown in Figs. 11(d)–11(f)) at different We . The color maps are scaled proportional to the inflow velocities. The insets in (j)–(l) show the corresponding averaged column shapes at the $z = 1.0$ cm plane. No significant deviations of the instantaneous shapes from the averaged shapes are observed.

origin of the surface instability that leads to the formation of these windward surface waves in liquid jets in crossflow. On one side, the growth of the waves has been explained in terms of Rayleigh-Taylor (R-T) instability caused by the interaction of the acceleration imposed by the pressure gradient (which is linked to the gas Weber number) at the front of the column with the interface density gradient.^{7,9,70} In such analyses,^{7,72} the wavelength with the maximum temporal growth was calculated from the R-T dispersion relation modified by the stabilizing effects of surface tension at high wave numbers (or small wavelengths). The outcome of the analysis was an expression of the form of $\lambda_s \propto We^{-n}$ with $n = 0.5$, which is consistent with what was observed in the experiments^{7,9} and also matched by the simulations in this work as shown in Fig. 3(a). A recent theoretical work using a different form of aerodynamic acceleration also supported a relation $\lambda_s/d_0 = 3.84We^{-0.5}$ between the wavelength and the Weber number,⁷¹ which is very similar to the experimental correlation Eq. (6).

On the other side, Proper Orthogonal Decomposition (POD) analysis of another set of experiments of liquid jets in cross-flow over a range of Weber numbers suggested that Kelvin-Helmholtz (K-H) instability due to the tangential velocity difference in liquid and gas phases (which for a

given liquid injection velocity is linked to the gas Weber number) is the driving mechanism for the wave development observed in the experimental images.⁶ In fact, the wavelength resolved by the experimental images in Ref. 6 was on the order of $\lambda_s/d_0 \sim 6$, much larger than the wavelengths witnessed in the current study.

As a first step in reconciling this apparently contradictory evidence in the literature, we establish the wavelength of the K-H instability for the problem under investigation here and compare it to the R-T instability predictions noted above. With this we aim to eliminate the rare possibility that the wavelengths arising from the two types of instability at the conditions of interest are similar. Based on the stability analysis for inviscid flow near a planar liquid-gas interface with discontinuous tangential velocities,⁷³ at the injection orifice where $U_g = 0$ and considering $\rho_l \gg \rho_g$, we obtain $\lambda_s/d_0 = 3\pi r_\rho (qWe)^{-1}$. A more complex linear analysis for a cylindrical surface taking account of all the relevant physics including viscosity was provided by Reitz.^{23,74} The predictions of wavelength for three different Weber numbers using both K-H^{73,74} and R-T expressions^{7,71} are summarized in Table V. At lower We (We = 10 and We = 40), the predicted values of wavelength based on the K-H expressions are much larger than the values based on the R-T expression and the experimental data. At higher We (We = 160), the predictions from both instabilities become much more similar suggesting that it would be difficult to distinguish the two in this range and providing the first evidence that the observed instability characteristics may depend on conditions. The disparity in the wavelengths at lower Weber numbers, however, is significant enough to clarify that at least for these conditions, formation of windward surface waves is due to the R-T instability.

This, however, does not necessarily imply that R-T is dominant in all liquid jets in crossflow. It is well established, for example, that in the absence of cross-flow, liquid jets get destabilized through K-H instability.⁷⁵ It is logical to expect that for small values of cross-flow velocity the jet should behave more like a jet in the absence of cross-flow and manifest K-H instability. That is, it is reasonable to expect that a transition from K-H to R-T instability exists as the cross-flow velocity is increased. For given fluids this transition point is likely dependent on the velocity ratio between the jet and the cross-flow. Thus, as was implied before, it is possible that either type of instability could be present depending on conditions. To shed more light on this, it is important to understand how the cross-flow weakens the K-H instability. To do this we consider the evolution of the jet velocity profile along the column trajectory “s” on the windward side of column as shown in Fig. 13(a). As the gas phase is accelerated along the trajectory “s,” the liquid phase velocity remains mostly unchanged (maybe slightly decelerated) (Fig. 13(b)). As a result, the absolute value of velocity difference (the dominant parameter that drives the K-H instability) decreases along “s” until it reaches to zero and then changes sign. Concomitantly, the out of plane vorticity also changes sign at the zero shear point (Fig. 13(c)). Therefore it is to be expected that K-H is progressively weakened in the region prior to the zero shear point and that the wavelength computed at the injection point represents the lower-bound estimate of any possible K-H waves emanating from this region. It is worth pointing out that analogous arguments indicate that an increased possibility of K-H exists after the zero shear point as the velocity difference increases. It should be clear, however, that such an instability would lead to waves that rotate in the opposite direction (clockwise in x-z plane) to those formed by K-H instability arising from the region prior to the zero shear point (counterclockwise in x-z plane). This, however, is not supported by the experimental or high fidelity simulation evidence. Indeed, for all cases we had access to (including those of Ref. 6) the waves

TABLE V. Surface wavelength λ_s/d_0 predicted using different linear instability analysis/correlation.

We	10	40	160
Kelvin Helmholtz analysis by Chandrasekhar ⁶⁵	9.02	2.25	0.56
Kelvin Helmholtz analysis by Reitz ⁶⁶	4.01	2.06	0.60
Rayleigh Taylor analysis by Wang <i>et al.</i> ⁶³	1.22	0.61	0.30
Experimental correlation by Sallam <i>et al.</i> ⁵	1.21	0.65	0.35

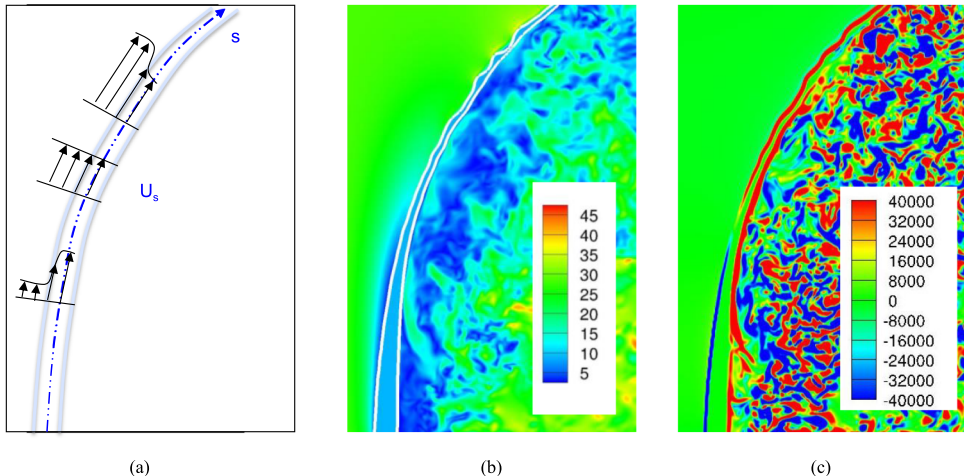


FIG. 13. (a) A schematic showing the evolution of tangential velocity profiles along the column trajectory “s” on the windward side of column. The absolute value of velocity difference decreases along “s” until it reaches to zero and then changes sign. Such changes in velocity profile are confirmed in the plot of the magnitude of X-Z in-plane velocity in (b). Concomitantly, the out of plane vorticity also changes sign at the zero shear point as shown in (c).

and resulting non-linear flow in the whole atomization region exhibited counterclockwise rotation as viewed in the x-z plane. This indicates that the destabilization of the flow occurs close to the injection point and prior to the zero shear point for these cases.

Another key issue to consider in this discussion is the fact that R-T is an absolute instability while K-H is a convective instability. As a result, the growth of the latter is strongly dependent on the perpetual introduction of upstream perturbations. The special care taken in the physical problem analyzed in this paper (both in the experiment and simulation) to eliminate inlet turbulence effects, which can act as sources of such perturbations, may have disadvantaged the K-H instability with respect to the R-T. It is reasonable to expect that if the inlet turbulence was further increased a regime may be reached that this turbulence completely drives the atomization process bypassing both the instability modes considered in this discussion.

So, in summary, we believe that the evidence in this work and in the rest of the literature can be reconciled under the hypothesis that liquid jets in cross-flow may exhibit either R-T or K-H instability or even neither of them depending on operating conditions and inlet turbulence levels. At moderate values of inlet turbulence one would expect a shift from K-H to R-T near the injector orifice as the gas Weber number increases and inlet turbulence effects are diminished. Verification of this hypothesis should be the subject of future work.

Another important atomization process occurs at the edge of liquid column where ligaments are pulled off the column at high shear and further break up into fine droplets. At increasing We (increasing velocities and shear rate), the location along the column to reach a critical point at which stripping is initiated decreases as shown in Fig. 3(b). In Fig. 10, at the $z = 0.25$ cm plane, stripping has not started for all three cases. At the $z = 0.5$ cm plane, stripping has not occurred for $We = 10$ and $We = 40$ and the $We = 160$ case might show first sign of stripping. At the $z = 0.75$ cm plane, stripping has started for the $We = 40$ case as well and intensive stripping of liquid off the column occurs for $We = 160$. This trend in the change of stripping onset location also has an impact on the 2D cross-section column shapes in the z-plane, as also shown in Fig. 12 (white curves). At $We = 160$ with increasing z , the column shape gradually changes to a “kidney” shape, consistent with the findings in the literature,³ which is caused by the stripping induced liquid depletion. However, at $We = 10$, the column changes to a more flat shape with conserved area or mass with little liquid stripped off, as reflected by the higher deformation values at $We = 10$ in Fig. 3(c). It is also observed that stripping preferentially occurs on the maximum peak of the surface waves (see Figs. 4(d) and 4(g)) where ligaments with relatively large radius of curvature (or small surface tension force) are stripped off the column and further break up into droplets. Therefore, the decreases in surface

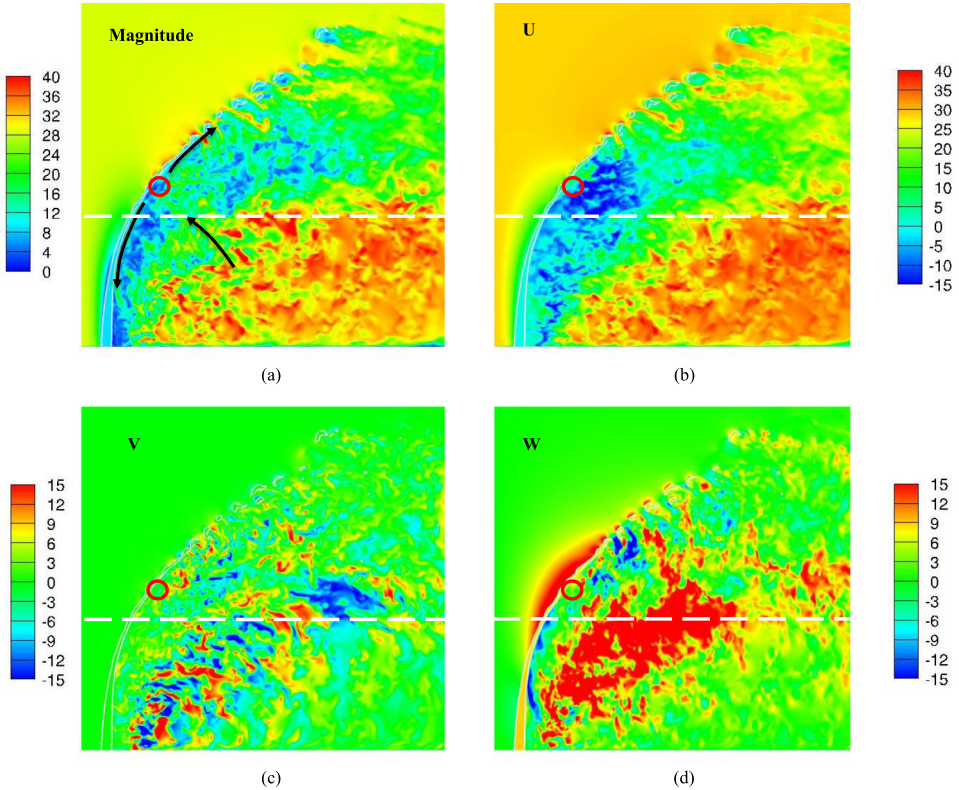


FIG. 14. The instantaneous surface shapes together with velocity magnitude and component contours at $y = 1$ cm plane, $We = 10$. The black arrows denote the direction of flow recirculation. The red circles denote the location of a stagnation point. The white dashed lines indicate the location of $z = 1$ cm planes to be shown next in Fig. 15.

wavelength with increasing We (Fig. 3(a)) also enhance the stripping breakup by providing more candidate locations for stripping. At the same z planes, the $We = 10$ case experiences much less (or more delayed) stripping, therefore the contiguous liquid continues to widen in the transverse direction (Fig. 11(d)). Due to the earlier and more intensive stripping for higher We cases, the liquid core is depleted earlier as shown by the reduced width with increasing We in Figs. 11(d)–11(f) (back curve). The reduction in column width at higher We leads to less blockage to the gas flow and less jet deflection as shown in Figs. 11(a)–11(c) (black curve). The earlier depletion of liquid core at higher We also leads to lower breakup locations as shown in Fig. 3(d).

As the liquid is depleted by stripping and the column gets deformed by aerodynamic forces for the $We = 160$ case, the liquid column becomes thinner as the jet penetrates into the crossflow. The amplitude of the column waves increases and becomes large enough to cause the fracture of the column into large chunks of liquid and ligaments (Figs. 10(f) and 10(i)). The high shear at high We leads to fast breakup (so-called “secondary breakup”) of these large liquid chunks into smaller droplets that are transported downstream. The insets of Figs. 10(a)–10(c) zoom into the detailed column and secondary breakup process occurring at the column end (upper left insets) as compared to the stripping process occurring at the column-surface (lower-right insets). For the higher Weber number cases ($We = 40$ and 160), at the column-surface liquid ligaments are formed and pulled off the main column and the ligaments further break up into droplets, while at the column end large chunks of liquid are broken off the main column and the liquid chunks break up into smaller droplets with much less formation of long ligaments. For the $We = 10$ case, stripping does not occur as early and the surface waves finally change into two concave liquid structures with three thick streaks continuously elongating at the edges and in the middle plane and two membrane thinning in-between (Figs. 10(d) and 10(g)). Note that the peculiar “three-streak-two-membrane” structures were not reported in the experimental study⁹ most likely due to the inability of cameras to capture

the front view. As discussed next, the development of the two membranes instead of one can be linked to the formation of recirculation zones behind the jet column. Note that the side-view “bags” observed in the experiment refer to the very thin liquid membrane before breakup, which cannot be resolved beyond a certain thickness by the grid resolution in the current simulation. As pointed out earlier, the fluid dynamics scale may be so small that any continuum-based simulation approach neglecting molecular physics will have challenges to faithfully simulate the process. However, the larger-scale processes towards bag breakup are still captured by the simulation with three thick streaks formed at the edges and the mid-plane enclosing the membranes in-between. These thick ligaments further break up into large-size liquid droplets (see Figs. 10(d) and 10(g)). Because of low We, these liquid droplets experience much less secondary breakup. The large Stokes number (the ratio of droplet relaxation time to flow characteristic time) for the large-size liquid droplets leads to further penetration (Fig. 11(a)) and spreading (Figs. 11(d) and 10(g)) of the spray. In contrast to the low We case, the smaller Stokes number associated with the smaller droplets for the higher We cases causes the droplets to change their velocity to be more aligned with the crossflow direction (Figs. 11(b), 11(c), 11(h), and 11(i)). Note that although the reduced column deflection at higher We tends to cause higher liquid penetration, the smaller droplets at higher We change the liquid trajectory and cause lower liquid penetration beyond the column breakup point (Figs. 11(a)–11(c)).

2. Gaseous flow near liquid column: Recirculation zone related to jet breakup

Figs. 14 and 15 display instantaneous pictures of the flow field for the We = 10 case in the $y = 1.0$ cm plane and $z = 1.0$ cm plane, respectively. On the windward side of the liquid jet, due to the aerodynamic blockage of the jet, a vertical zone with reduced U velocity is formed (Figs. 14(b) and 15(b)). The blocked gas flow goes around the jet by accelerating in the transverse direction (Fig. 15(c)) and in the penetration direction (Fig. 15(d), red zone on the windward size). The low pressure behind the jet causes the flow to recirculate back as shown by the black arrows in

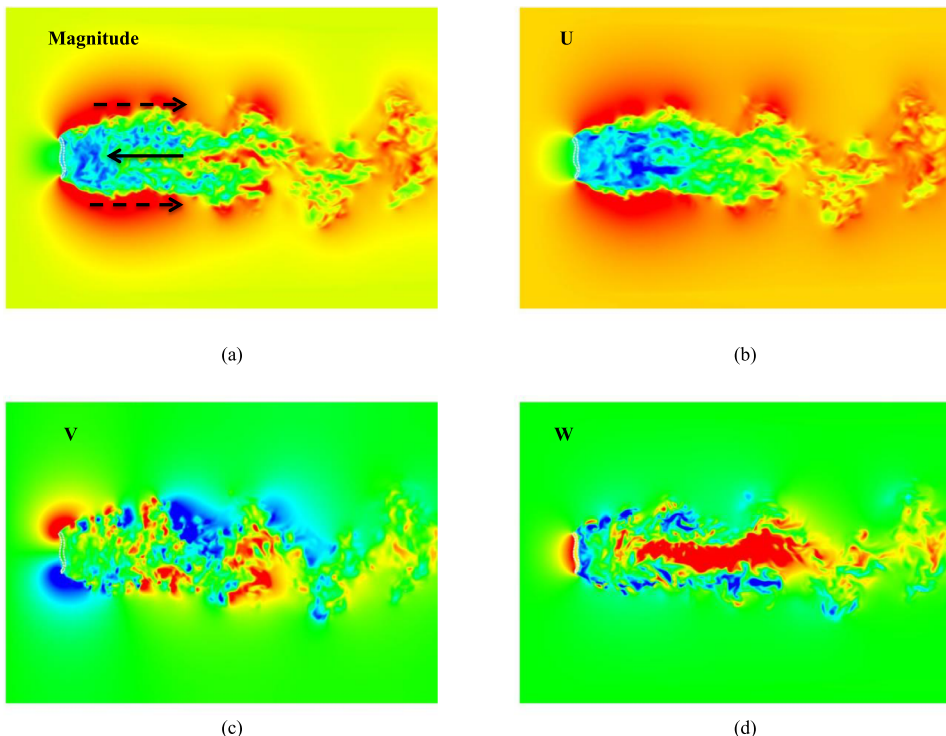


FIG. 15. The instantaneous surface shapes together with velocity magnitude and component contours at $z = 1$ cm plane (shown in Fig. 14), We = 10. The black arrows denote the direction of flow recirculation. The solid arrow indicates flow going above the plane and the dashed arrow indicates flow going below the plane. The color maps are the same as in Fig. 14.

Figs. 14 and 15. A negative (represented by “blue” color) U in Fig. 14(b) and positive (represented by “red” color) W in Fig. 14(d) indicate the left-upward direction of flow in Fig. 15(a). When the recirculated flow reaches the leeward surface of the liquid jet, the flow is diverted into two streams in the mid plane: a right-upward stream and a left-downward stream shown in Fig. 14(a). The left-downward stream near the leeward surface can be observed by the “blue” zone for U in Fig. 14(b) and the “blue” zone for W in Fig. 14(d). The negative U and W for the left-downward stream can be also observed in Figs. 15(b) and 15(d). The right-upward stream near the leeward surface can be observed by the light green zone in Fig. 14(b) and green/red zone in Fig. 14(d). All these observations suggest that a stagnation point exists where the flow diversion occurs. In the transverse direction, the combination of U and V in Figs. 15(b) and 15(c) suggests two recirculation bubbles are present in the wake region. The flow is in the positive x direction on the outer edge of the wake and in the negative x direction in the center of the wake. Therefore, a complete picture of the recirculation flow structure can be sketched in Fig. 16. The flow is consistent with the typical recirculation flow behind a bluff body. Because of the bending, the liquid jet is not strictly perpendicular to the crossflow, and the recirculation flow becomes three-dimensional in nature. Instead of a stagnation line in 2D, a stagnation point is formed for the 3D case. Two vortex tubes with opposite vorticity directions are formed and they are more or less aligned with the liquid jet orientation.

The recirculation flow structures at different We are compared in Fig. 17. Plots of averaged velocity magnitude are shown and the color map is scaled in proportion to the inflow velocity to better compare the flow structures for different cases. The center of the recirculation flow is indicated by the locations with zero averaged velocity magnitude. At least two diverted recirculation flow structures can be identified on the leeward side of the liquid jet: one tightly attached to the liquid jet close to the injection orifice and the other further downstream. The stagnation points can also be identified as the point with zero averaged velocity magnitude. It can be observed that as We increases, the recirculation zone shrinks and the stagnation points move toward the injection orifice. This is probably due to the reduced column width (Figs. 11(d)-11(f)) and therefore reduced blockage effects as We increases. The differences in jet column physics not only affect the location

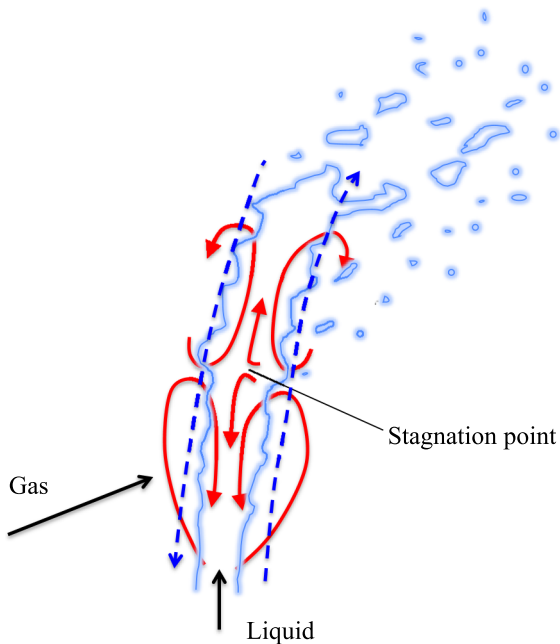


FIG. 16. A schematic of the averaged flow recirculation and vortical structures in the wake region behind the liquid jet. Red solid curves indicate the flow direction and dark blue dashed curves indicate the vortex tube direction, which all reside behind the liquid column outlined by light blue color. The liquid jet is not strictly perpendicular to the crossflow, and the recirculation flow is three-dimensional in nature. A stagnation point and two vortex tubes with opposite vorticity directions are formed.

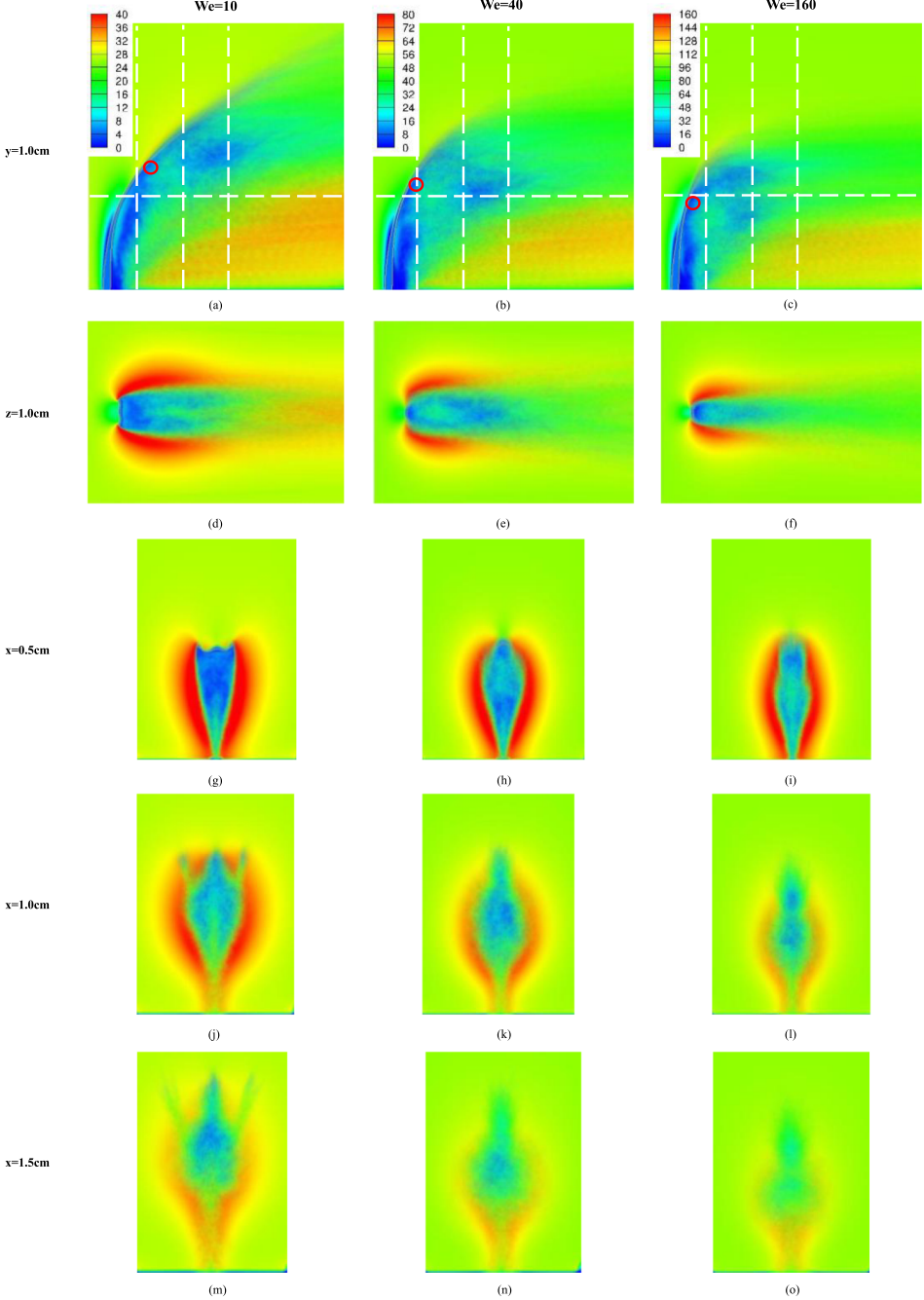


FIG. 17. Comparison of the averaged velocity magnitude at several planes for different We . The red circles denote the locations of stagnation points. The white dashed lines indicate the locations of other planes. The color maps are scaled proportional to the inflow velocities. The time periods for averaging are 4 ms for $We = 10$, 2 ms for $We = 40$, and 1 ms for $We = 160$. The center of the recirculation flow is indicated by the locations with zero averaged velocity magnitude. Two diverted recirculation flow structures can be identified on the leeward side of the liquid jet: one tightly attached to the liquid jet close to the injection orifice and the other further downstream. The stagnation points can also be identified as the point with zero averaged velocity magnitude.

of recirculation but also lead to the differences in downstream flow profiles as shown in the different z planes in Fig. 17, as related to differences in vortex shedding discussed next.

One question that emerges in Figs. 10 and 11 is why a contiguous thick ligament is formed in the mid-plane, especially for the $We = 10$ case that forms two bags on each side in-between three

ligaments. This peculiar liquid structure is a direct consequence of the flow recirculation behind the jet, and a complex two-way interaction between jet breakup and gaseous flow. Because of the presence of recirculation streams in the y mid plane towards the leeward surface of the liquid jet (Fig. 14(a)), the transverse stretching of liquid membrane in the middle is suppressed at the y mid plane. As a result of the recirculating flow structure (Fig. 16), a long mid streak of liquid is formed, causing the formation of two bags on each side. Much less impact of recirculation on the mid plane liquid structure is observed at higher We , because of the depletion of liquid by stripping and the reduction of column width. It is interesting to note that the three ligament or streamer structure was also observed at low We in a recent experiment of liquid jet in cross flow (e.g., the $We = 29$ case in Ref. 18). The physical origin of such phenomena was not conclusively determined from the experimental data. Current simulation study provides a reasonable explanation for the three-streamer phenomenon observed in the experiment.

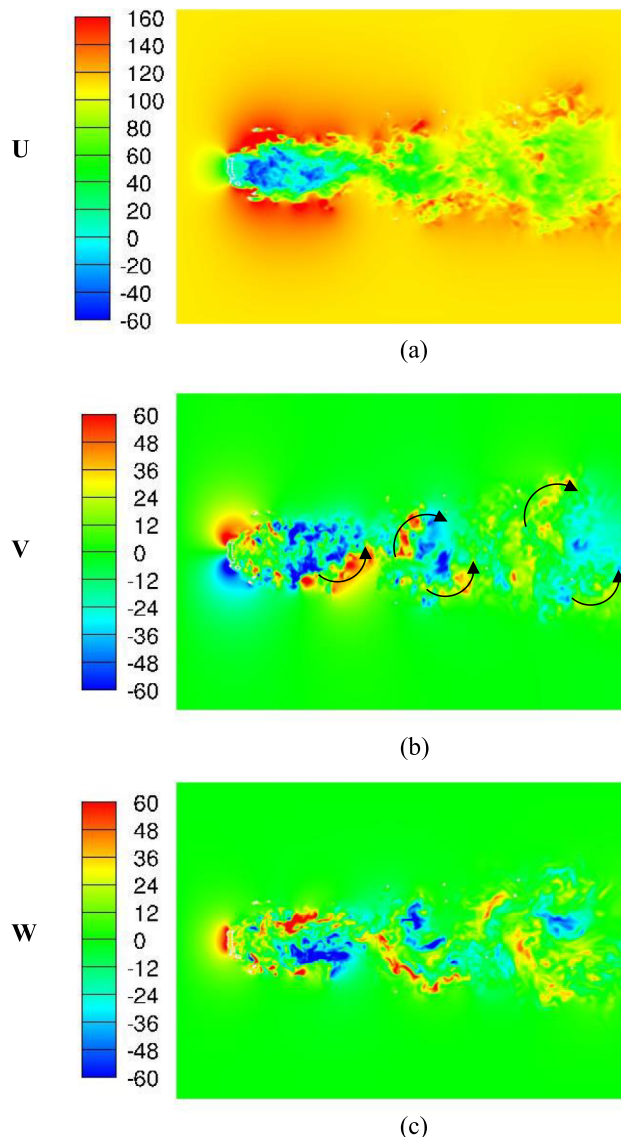


FIG. 18. Instantaneous velocity component contours at $z = 1.0$ cm plane, $We = 160$. The flow patterns very much resemble a von Karman vortex structure behind a bluff body. While the amplitude of the von Karman oscillations is shown to increase downstream, the magnitude of the velocity components decreases due to vortex dissipation. Because of the three-dimensional nature of the atomization flow, the W velocity also shows a periodic pattern in (c), indicating the shedding of a three-dimensional vortical flow from the jet column.

3. Gaseous flow: Von Karman vortices downstream of liquid column

To demonstrate the far-field vortical flow structures behind the liquid jet, an instantaneous snapshot of the velocity components for the $We = 160$ case at the $z = 1.0$ cm plane is shown in Fig. 18. Combining U and V component, recirculation flows in opposite directions with spatial periodicity can be identified as shown in Fig. 18(b). The flow patterns very much resemble a von Karman vortex structure that can be attributed to a periodic shedding of vortices of opposite sign behind a bluff body,⁷⁶ which occurs when the Reynolds number is larger than a critical value depending on the size and shape of the bluff body. While the amplitude of the von Karman oscillations increases downstream in Fig. 18, the magnitude of the velocity components decreases due to vortex dissipation. Because of the three-dimensional nature of the atomization flow, the W velocity also shows a periodic pattern in Fig. 18(c), indicating the shedding of a three-dimensional vortical flow. The temporal evolution of the vortical flow can be analyzed using a series of snapshots. In Fig. 19,

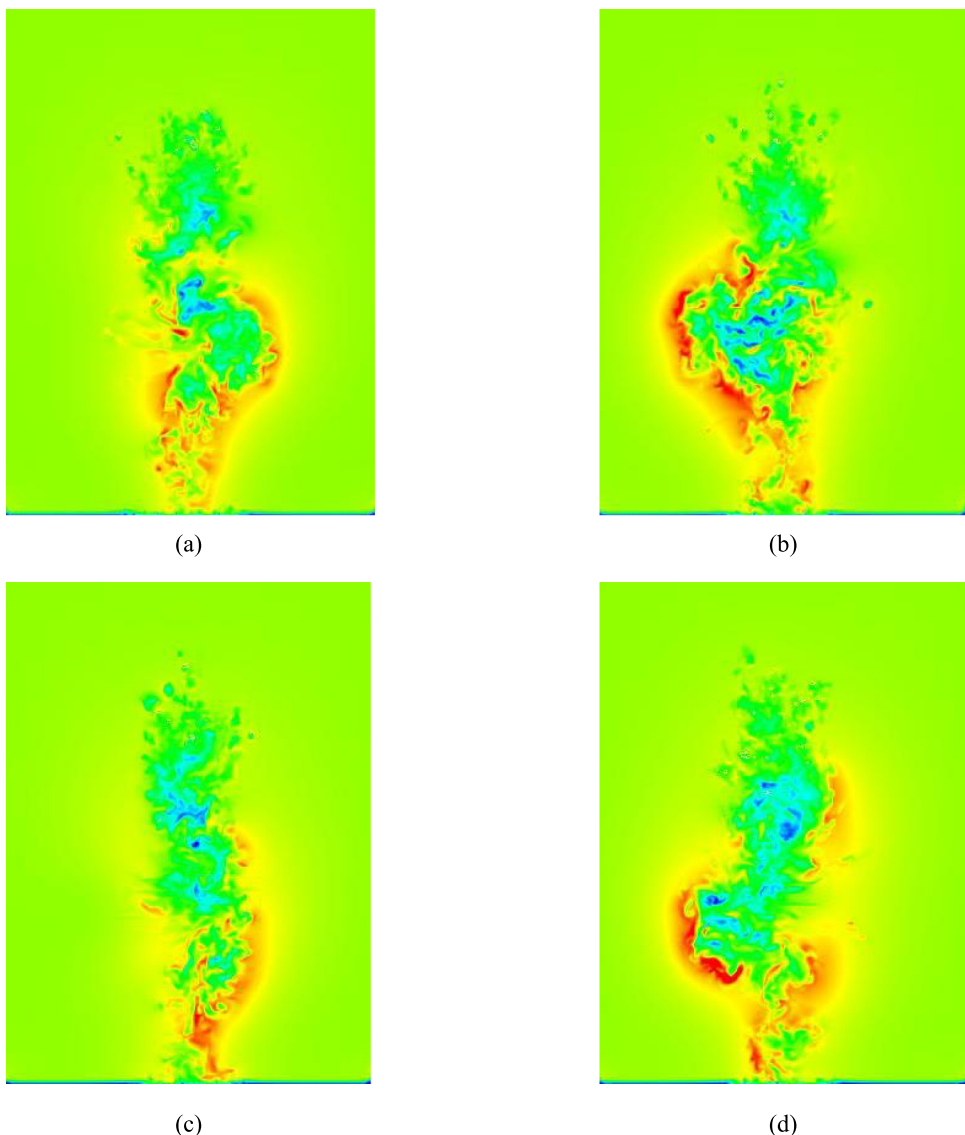


FIG. 19. Instantaneous velocity magnitude contours at $x = 1.5$ cm plane at several different instants, (a) $t = 1.54$ ms, (b) $t = 1.6$ ms, (c) $t = 1.66$ ms, (d) $t = 1.72$ ms, $We = 160$. The color maps are the same as in Fig. 17(c). The intervals of these snapshots are selected so that the flow is repeating similar patterns, with (a) similar to (c) and (b) similar to (d), but (a) and (c) opposite to (b) and (d).

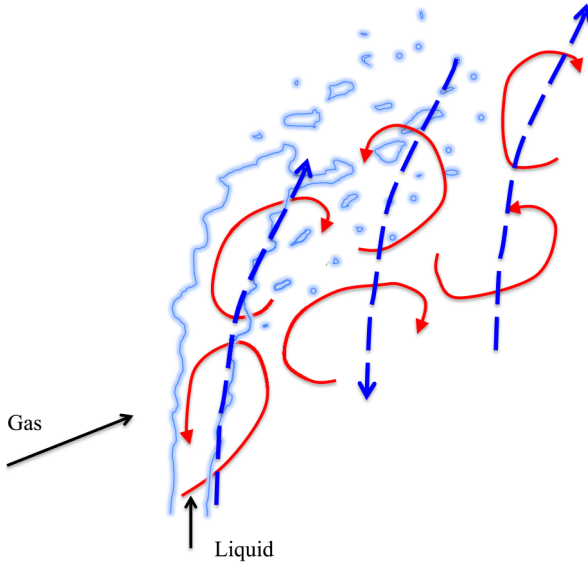


FIG. 20. A schematic of the unsteady three-dimensional vortex street structure behind the liquid jet is shown. Red solid curves indicate the flow direction and dark blue dashed curves indicate the vortex tube direction, which all reside behind the liquid column outlined by light blue color. The temporal evolution of the flow shows a periodic shedding of vortices and a periodic dominance of one vortical flow over the other with an opposite sign, leading to an asymmetric instantaneous flow field.

snapshots of the velocity magnitude for the $We = 160$ case at the $x = 1.5$ cm plane at different instants confirmed the dynamic change in flow structures. The intervals of these snapshots are selected so that the flow is repeating similar patterns, with (a) similar to (c) and (b) similar to (d), but (a) and (c) opposite to (b) and (d). A picture of the unsteady three-dimensional flow structures can be sketched as in Fig. 20. Although the averaged flow fields (Fig. 17) show a symmetric flow structure with two recirculating bubbles behind the jet, the temporal evolution of the flow shows a periodic shedding of vortices and a periodic dominance of one vortical flow over the other with an opposite sign, leading to an asymmetric instantaneous flow field as in Fig. 19. As shown in Fig. 16, vortex tubes aligned with the jet orientation are formed. The axis of the vortex flow in the upper part is more aligned with the x -axis instead of the z -axis. Because of the bending of vortex tubes into the x -direction, the vortices evolve into different oscillation behaviors in the upper part of the flow than the lower part, as shown in Fig. 19.

Using the POD approach to analyze a temporal series of flow images, we can quantitatively extract the frequencies that characterize the flow dynamics for the three different We cases. The behavior of two-dimensional von Karman vortex behind a cylinder is governed by⁷⁶

$$St = \frac{fD}{U_g} = 0.198(1 - \frac{19.7}{Re_D}), \quad (19)$$

where St is the Strouhal number, f is the vortex shedding frequency, D is the diameter of the cylinder, U_g is crossflow velocity, and Re_D is the Reynolds number based on cylinder diameter. Although the vortex structures behind the liquid jet show strong three-dimensionality (Fig. 20), it is still interesting to see whether the 3D vortex structures follow similar frequency responses as the two-dimensional vortex structures behind a cylinder. Figs. 21(a)-21(f) show the pairs of the most energy containing POD modes and the corresponding power spectral density for the $z = 1.0$ cm plane velocities. The mode pairs share the same frequencies identified by the maximum peaks of the power spectral density, indicating the presence of a traveling wave of vortices. These frequencies dictate the vortex shedding frequency. In Figs. 21(g)-21(l), the POD analyses of $x = 1.5$ cm plane velocity reveal the presence of a flow oscillation as 3D vortex tubes pass through the plane. The oscillation frequencies are also extracted based on the maximum peaks in the power spectral density plot. All the extracted frequencies are listed in Table VI. For $We = 40$ and 160, the oscillating

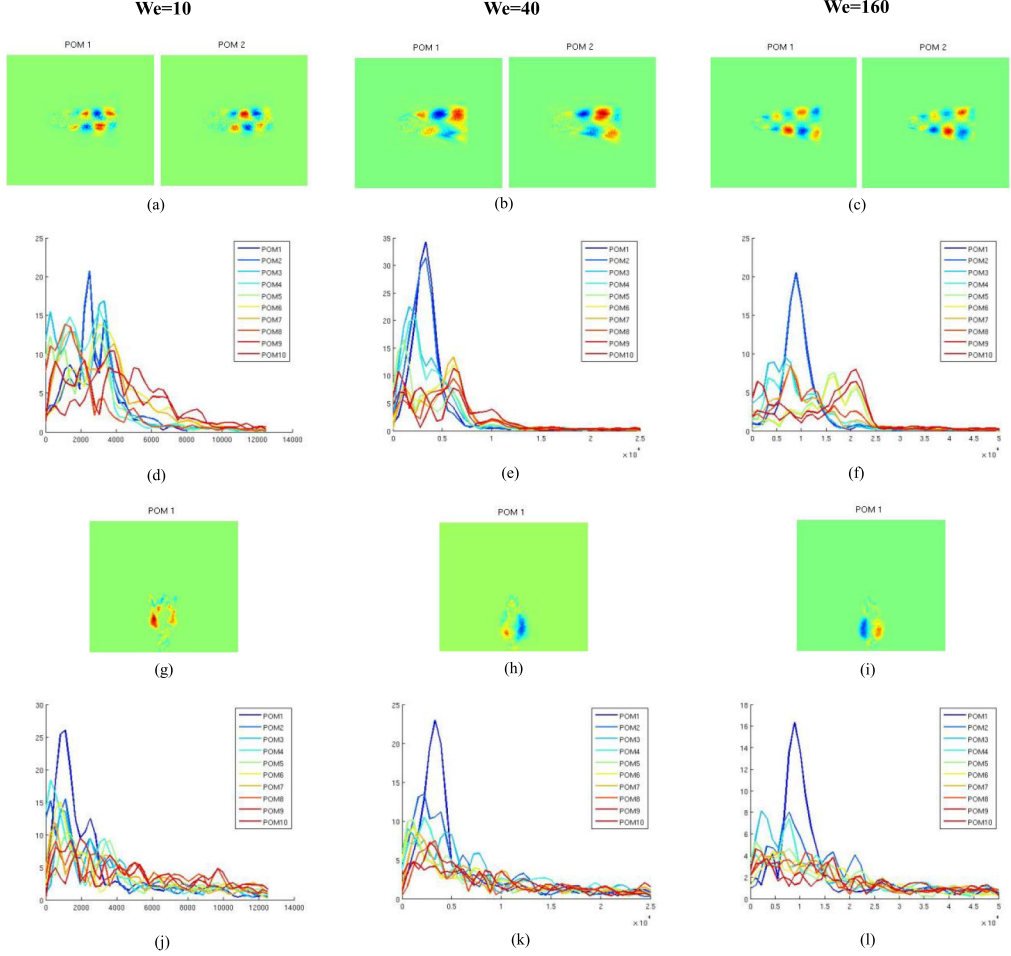


FIG. 21. (a)–(c) show the pairs of the most energy containing POD modes for velocity magnitude contours in the $z = 1.0$ cm plane for different We . (d)–(f) show the corresponding power spectral density (PSD) for different We . The mode pairs share the same frequencies identified by the maximum peaks of the power spectral density. (g)–(i) show the most energy containing POD mode for velocity magnitude contours in the $x = 1.5$ cm plane for different We . (j)–(l) show the corresponding power spectral density (PSD) for different We . The oscillation frequencies are also extracted based on the maximum peaks in the power spectral density plot. All the extracted frequencies are listed in Table VI.

frequency in the $x = 1.5$ cm plane and the wave frequency in the $z = 1.0$ cm plane match and their values are shown in Table VI. For $We = 10$, a higher frequency is captured in the $z = 1.0$ cm plane than in the $x = 1.5$ cm plane. Currently, the physical origin of the differences in the two frequencies is not clear. The averaged column width at the $z = 1.0$ cm plane in Figs. 17(d)–17(f) can be used as a representative diameter for the bluff body as listed in Table VI as well. As shown in Table VI, increases in We (or flow velocity U) lead to increases in shedding frequency and decreases in column width. The St for simulations at different We is computed to be a constant $St_{\text{sim}} = 0.118$ independent of We . It is different than the theoretical value of $St_{\text{theory}} = 0.198$ for two-dimensional flow past a cylinder. The difference is probably due to the different obstacle shapes (deformed column vs. cylinder) and the different flow dimensionality (3D vs. 2D).

It is interesting to further explore to what extent droplets respond to the von Karman flow oscillations at their inherent frequencies. The maximum time scale for the minimum frequency observed in the $We = 10$ case is around $t_{vk} = 1$ ms. For a droplet with Stokes number

$$Sto = \frac{\rho_l d_p^2}{18 \mu_g t_{vk}} \quad (20)$$

TABLE VI. Strouhal number computed for unsteady vortical structure behind liquid jet.

We	10	40	160
f (s^{-1})	1111 (2500) ^a	3333	8888
D (m)	0.0029	0.00194	0.00145
U_g (m/s)	27.4	54.8	109.6
St_{sim}	0.118 (0.2645) ^a	0.118	0.118
Re_D	5041	6745	10082
St_{theory}	0.197	0.197	0.198

^aThe frequency and St in the brackets are value based on POD analysis of $z = 1.0$ cm plane for We = 10.

to be 1, the droplet size d_p is calculated to be 18 μm . Since the minimum droplet size reported in the experiments and captured in the current simulations is around 40 μm (see Fig. 7), and a large fraction of droplets have sizes larger than 100 μm (especially for those formed by column fracture at the jet tip region), the corresponding droplet Stokes numbers are typically much larger than 1. As a result, most of the droplets are not expected to respond significantly to the downstream von Karman flow oscillations. As shown in Figs. 10(g)–10(i), little large scale periodic motion of droplet clouds is observed in comparison to the periodic oscillation of gas flow as shown in Figs. 15, 18, and 19. Note that unresolved droplets below $\sim 18 \mu\text{m}$ scale may be present in reality and may have significant response to the gas dynamics, although their total volume fraction is expected to be small.

Finally, it is also worth noting that the periodic shedding of vortices usually provides a feedback to the obstacle body by introducing a periodic oscillation of the nearby pressure field and causing the obstacle to vibrate sideways when the forcing frequency and its sub-harmonics match the natural frequency of the obstacle. However, such type of impact of oscillating flow on the liquid jet is not observed and the jet column in Figs. 10(d)–10(f) also shows little lateral oscillations.

IV. SUMMARY AND CONCLUSIONS

In this paper, a first-ever detailed validation of high-fidelity simulations of liquid jet atomization in gaseous crossflow at ambient conditions is presented and a comprehensive investigation of the two-phase flow underlying physics is described. A suite of state of the art computational algorithms (CLSVOF, Ghost Fluid, AMR, Eulerian-Lagrangian droplet mapping) was leveraged to overcome the accuracy and stability challenges in such simulations. High performance computing involving thousands of processors was employed to make the high-cost parallel computations tractable. The simulations were conducted at ambient conditions (liquid to gas density ratio of 845) in a well-defined setup closely matching the conditions of a select experiment that focused on the impact of aerodynamic forces on atomization by eliminating inlet turbulence effects. Three cases in the intermediate Weber number range (We = 10–160) were simulated. The grid spatial resolution was set to capture the smallest experimentally observed liquid lengthscale and the temporal resolution was constrained by a classical CFL and a surface tension based criteria.

Simulation results match the experimental observations of liquid column details as well as the formation of droplets. Comparisons were made on features such as the windward column wavelength, column deformation, stripping onset location, and column breakup locations that exemplify the instability development on the liquid column. The minor discrepancies between simulation and experiment were found to be well within the uncertainty range of the experimental data. A similar degree of experimental matching was achieved by simulations using either uniform grid or interfacial adaptive mesh refinement, indicating the equivalence of the two grid configurations in capturing interfacial instabilities and breakup. Droplets initially formed near the liquid column as measured in the experiment were also compared with the simulation results extracted using a specialized

transformation technique. The droplet size, velocity, and formation rate of these droplets were found to be in good agreement with the experiment mostly in the shear breakup regime.

The validated simulation data were used in a thorough exploration of the physics of jet atomization interacting with the gas flow. A notable “ Λ ” shape of windward column waves was observed for the first time and explained by the combined effects of upward and transverse surface traveling motion. Instability mechanisms for the initiation of windward column waves were explored. Rayleigh-Taylor instability was verified as the primary mechanism for generating the windward waves due to the fact that its predicted wavelength better matches the experimental and simulation data for the Weber numbers considered in this study. Using physical arguments it was postulated that this result may be due to the specific operating and boundary conditions employed in this study (Weber number and the inlet turbulence were specifically pointed out) and that it would be possible that under different conditions liquid jets in cross-flow which owe their destabilization to Kelvin-Helmholtz instability could exist. The notion of experimentally observed leeward waves was clarified as the formation of ligaments/droplets at the transverse edge of the column due to the surface instability and stripping. The impact of Weber number on the stripping of droplet from the transverse edge of the column was investigated and linked with the windward surface waves. It was found that shorter wavelength at higher Weber number promotes ligament formation and droplet stripping by providing more higher-curvature surface candidates. In the later part of liquid column, a peculiar “three-ligament-two-membrane” structure was observed for the first time and explained as the outcome of the formation of symmetric recirculating bubbles for the gas flow behind the jet column. The three-dimensional recirculating wake flow was investigated in detail and related to the formation of a three-dimensional von Karman type vortical flow structure further downstream. The frequency contents of such vortical flows were quantified. It was shown that the time scale for gas flow oscillations is much smaller than the relaxation time for the typical droplets and the droplets are effectively unresponsive to gas flow oscillations for the conditions studied.

In closing, it is our hope that the results presented in this paper exemplify the potential of high fidelity simulation as an analysis tool in the area of spray atomization. Specifically, such simulation enables a unique opportunity to extract three-dimensional flow information and insight not easily accessible through two-dimensional experimental images or measurements. Given this advantage, we expect that high fidelity simulation will become an increasingly common research tool in this area.

ACKNOWLEDGMENTS

The authors wish to acknowledge the funding support from United Technologies Corporation. Thanks and appreciations are also extended to Professor Mark Sussman for many helpful insights on the numerical aspects of the work and for access to his CLSVOF algorithm several years ago. Finally, this work would not have been possible without the computer resources and staff assistance from the Oak Ridge Leadership Computing Facility at Oak Ridge National Laboratory, which is supported by the Office of Science of the Department of Energy under Contract No. DE-AC05-00OR2272.

NOMENCLATURE

- A = Area,
- d = diameter,
- d_0 = injector orifice diameter,
- D = diameter of cylinder,
- \mathbf{D} = deviatoric strain rate tensor,
- f = frequency,
- F = volume of fluid,
- H = Heaviside function,
- \mathbf{I} = identity tensor,
- L = length scale,

\dot{m}'' = droplet formation rate,
 N = number of particles (droplets),
 p = flow pressure,
 q = momentum flux ratio,
 r_μ = viscosity ratio,
 r_ρ = density ratio,
 R = specific gas constant,
 Re = Reynolds number,
 St = Strouhal number,
 Sto = Stokes number,
 t = time,
 T = temperature,
 \mathbf{u} = velocity,
 U = imposed velocity,
 V = volume,
 We = Weber number,
 \mathbf{x} = coordinate,
 x = coordinate in direction of crossflow,
 y = coordinate orthogonal to x and z ,
 z = coordinate in direction of liquid injection,
 Δt = time step,
 Δx = grid spacing,
 ε = droplet formation efficiency,
 Φ = phase indicator function,
 φ = level set function,
 κ = curvature,
 λ = wave length,
 μ = dynamic viscosity,
 ν = kinematic viscosity,
 ρ = density,
 σ = surface tension.

Subscripts

b = Column breakup property,
 g = gas property,
 i = column onset property,
 l = liquid property,
 p = particle (droplet) property,
 s = surface property,
 vk = von Karman flow property,
 \min = minimum.

Superscripts

j = Particle j ,
 n = step n .

¹ P. K. Wu *et al.*, “Breakup processes of liquid jets in subsonic crossflows,” *J. Propul. Power* **13**(1), 64–73 (1997).

² Y. Huang and V. Yang, “Dynamics and stability of lean-premixed swirl-stabilized combustion,” *Prog. Energy Combust. Sci.* **35**, 293–364 (2009).

³ K. D. Kihm, G. M. Lyn, and S. Y. Son, “Atomization of cross-injecting sprays into convective air stream,” *Atomization Sprays* **5**, 417–433 (1995).

⁴ J. Mazallon, Z. Dai, and G. M. Faeth, “Primary breakup of nonturbulent round liquid jets in gas crossflows,” *Atomization Sprays* **9**(3), 291–311 (1999).

⁵ M. Herrmann, “Detailed numerical simulations of the primary atomization of a turbulent liquid jet in crossflow,” *ASME J. Eng. Gas Turbines Power* **132**(6), 061506-1–061506-10 (2010).

- ⁶ M. Arienti and M. C. Soteriou, "Time-resolved proper orthogonal decomposition of liquid jet dynamics," *Phys. Fluids* **21**(11), 112104 (2009).
- ⁷ C. L. Ng, R. Sankarakrishnan, and K. A. Sallam, "Bag breakup of nonturbulent liquid jets in crossflow," *Int. J. Multiphase Flow* **34**, 241 (2008).
- ⁸ P. K. Wu, L. K. Tseng, and G. M. Faeth, "Primary breakup in gas/liquid mixing layers for turbulent liquids," *Atomization Sprays* **2**, 295–317 (1992).
- ⁹ K. A. Sallam, C. Aalburg, and G. M. Faeth, "Breakup of round nonturbulent liquid jets in gaseous crossflow," *AIAA J.* **42**(12), 2529–2540 (2004).
- ¹⁰ J. C. Beale and R. D. Reitz, "Modeling spray atomization with the Kelvin-Helmholtz/Rayleigh-Taylor hybrid model," *Atomization Sprays* **9**(6), 623–650 (1999).
- ¹¹ E. V. Jens Eggers, "Physics of liquid jets," *Rep. Prog. Phys.* **71**, 036601 (2008).
- ¹² E. A. Kush and J. A. Schetz, "Liquid jet injection into a supersonic flow," *AIAA J.* **11**(9), 1223–1224 (1979).
- ¹³ A. S. Nejad and J. A. Schetz, "Effects of properties and locations in the plume or droplet diameter for injection in a supersonic stream," *AIAA J.* **21**(7), 956–961 (1983).
- ¹⁴ J. A. Schetz and A. Paddy, "Penetration of a liquid jet in subsonic airstreams," *AIAA J.* **15**(10), 1385–1390 (1997).
- ¹⁵ T. T. Nguyen and A. R. Karagozian, "Liquid fuel jet in a subsonic crossflow," *J. Propul. Power* **8**(1), 21–29 (1992).
- ¹⁶ M. A. Linnea, M. Paciaroni, E. Berrocalb, and D. Sedarsky, "Ballistic imaging of liquid breakup processes in dense sprays," *Proc. Combust. Inst.* **32**(2), 2147–2161 (2009).
- ¹⁷ M. Linne, M. Paciaroni, T. Hall, and T. Parker, "Ballistic imaging of the near field in a diesel spray," *Exp. Fluids* **40**(6), 836–846 (2006).
- ¹⁸ D. Sedarsky, M. Paciaroni, E. Berrocal, P. Petterson, J. Zelina, J. Gord, and M. Linne, "Model validation image data for breakup of a liquid jet in crossflow: Part I," *Exp. Fluids* **49**(2), 391–408 (2010).
- ¹⁹ L. P. Hsiang and G. M. Faeth, "Near-limit drop deformation and secondary breakup," *Int. J. Multiphase Flow* **18**(5), 635–652 (1992).
- ²⁰ L. P. Hsiang and G. M. Faeth, "Drop deformation and breakup due to shock wave and steady disturbances," *Int. J. Multiphase Flow* **21**(4), 545–560 (1995).
- ²¹ J. Becker and C. Hassa, "Breakup and atomization of a kerosene jet in crossflow at elevated pressure," *Atomization Sprays* **11**, 49–67 (2002).
- ²² P. J. O'Rourke and A. A. Amsden, "The TAB method for numerical calculation of spray droplet breakup," SAE Technical Paper 872089, 1987.
- ²³ R. D. Reitz and F. V. Bracco, "Mechanism of atomization of a liquid jet," *Phys. Fluids* **25**(10), 1730–1742 (1982).
- ²⁴ R. K. Madabhushi, "A model for numerical simulation of breakup of a liquid jet in crossflow," *Atomization Sprays* **13**(4), 413–424 (2003).
- ²⁵ J. Chesnel *et al.*, "Subgrid analysis of liquid jet atomization," *Atomization Sprays* **21**(1), 41–67 (2011).
- ²⁶ J. Chesnel *et al.*, "Large eddy simulation of liquid jet atomization," *Atomization Sprays* **21**(9), 711–736 (2011).
- ²⁷ R. Lebas *et al.*, "Numerical simulation of primary break-up and atomization: Dns and modelling study," *Int. J. Multiphase Flow* **35**(3), 247–260 (2009).
- ²⁸ P. Jenny, D. Roekaerts, and N. Beishuizen, "Modeling of turbulent dilute spray combustion," *Prog. Energy Combust. Sci.* **38**(6), 846–887 (2012).
- ²⁹ F. Xiao, M. Dianat, and J. J. McGuirk, "LES of turbulent liquid jet primary breakup in turbulent coaxial air flow," *Int. J. Multiphase Flow* **60**, 103–118 (2014).
- ³⁰ F. Xiao, M. Dianat, and J. J. McGuirk, "Large eddy simulation of single droplet and liquid jet primary breakup using a coupled level set/volume of fluid method," *Atomization Sprays* **24**(4), 281–302 (2014).
- ³¹ F. Xiao, M. Dianat, and J. J. McGuirk, "Large eddy simulation of liquid-jet primary breakup in air crossflow," *AIAA J.* **51**(12), 2878–2893 (2013).
- ³² M. Herrmann, "A sub-grid surface dynamics model for sub-filter surface tension induced phase interface dynamics," *Comput. Fluids* **87**(10), 92–101 (2013).
- ³³ J. A. Sethian and P. Smereka, "Level set methods for fluid interfaces," *Annu. Rev. Fluid Mech.* **35**, 341–372 (2003).
- ³⁴ O. Desjardins, V. Moureau, and H. Pitsch, "An accurate conservative level set/ghost fluid method for simulating turbulent atomization," *J. Comput. Phys.* **227**(18), 8395–8416 (2008).
- ³⁵ O. Desjardins and H. Pitsch, "A spectrally refined interface approach for simulating multiphase flows," *J. Comput. Phys.* **228**(5), 1658–1677 (2009).
- ³⁶ R. Scardovelli and S. Zaleski, "Direct numerical simulation of free-surface and interfacial flow," *Annu. Rev. Fluid Mech.* **31**, 567–603 (2003).
- ³⁷ G. Tomar *et al.*, "Multiscale simulations of primary atomization," *Comput. Fluids* **39**(10), 1864–1874 (2010).
- ³⁸ G. Tryggvason, B. Bunner, A. Esmaili, D. Juric, N. Al-Rawahi, W. Tauber, J. Han, S. Nas, and Y. J. Jan, "A front-tracking method for the computations of multiphase flow," *J. Comput. Phys.* **169**(2), 708–759 (2001).
- ³⁹ S. O. Unverdi and G. Tryggvason, "A front-tracking method for viscous, incompressible, multi-fluid flows," *J. Comput. Phys.* **100**(1), 25–37 (1992).
- ⁴⁰ M. Herrmann, "A balanced force refined level set grid method for two-phase flows on unstructured flow solver grids," *J. Comput. Phys.* **227**(4), 2674–2706 (2008).
- ⁴¹ T. Himeno, T. Watanabe, and A. Konno, "Numerical analysis for propellant management in rocket tanks," *J. Propul. Power* **21**(1), 76–86 (2005).
- ⁴² M. Sussman, K. M. Smith, M. Y. Hussaini, M. Ohta, and R. Zhi-Wei, "A sharp interface method for incompressible two-phase flows," *J. Comput. Phys.* **221**, 469–505 (2007).
- ⁴³ T. Menard, S. Tanguy, and A. Berlemont, "Coupling level set/VOF/ghost fluid methods: Validation and application to 3D simulation of the primary break-up of a liquid jet," *Int. J. Multiphase Flow* **33**(5), 510–524 (2007).
- ⁴⁴ J. Shinjo and A. Umemura, "Simulation of liquid jet primary breakup: Dynamics of ligament and droplet formation," *Int. J. Multiphase Flow* **36**(7), 513–532 (2010).

- ⁴⁵ O. Desjardins and H. Pitsch, "Detailed numerical investigation of turbulent atomization of liquid jets," *Atomization Sprays* **20**(4), 311–336 (2010).
- ⁴⁶ M. Herrmann, "The influence of density ratio on the primary atomization of a turbulent liquid jet in crossflow," in Proceedings of Combustion Institute, 2011.
- ⁴⁷ M. Herrmann, M. Arienti, and M. Soteriou, "The impact of density ratio on the liquid core dynamics of a turbulent liquid jet injected into a crossflow," *ASME J. Eng. Gas Turbines Power* **133**(6), 061501-1–061501-9 (2011).
- ⁴⁸ M. Behzad, N. Ashgriz, and B. W. Karney, "Surface breakup of a non-turbulent liquid jet injected into a high pressure gaseous crossflow," *Int. J. Multiphase Flow* **80**, 100–117 (2016).
- ⁴⁹ L. C. Vincent and P. Heinz, "A monotonicity preserving conservative sharp interface flow solver for high density ratio two-phase flows," *J. Comput. Phys.* **249**, 185–203 (2013).
- ⁵⁰ O. M. Desjardins, O. Jeremy, M. Owkes *et al.*, "Direct numerical and large-eddy simulation of primary atomization in complex geometries," *Atomization Sprays* **23**(11), 1001–1048 (2013).
- ⁵¹ S. Ghods and M. Herrmann, "A consistent rescaled momentum transport method for simulating large density ratio incompressible multiphase flows using level set methods," *Phys. Scr.* **T155**, 014050 (2013).
- ⁵² M. Raessi and H. Pitsch, "Consistent mass and momentum transport for simulating incompressible interfacial flows with large density ratios using the level set method," *Comput. Fluids* **63**, 70–81 (2012).
- ⁵³ M. Arienti, X. Li, M. C. Soteriou, C. A. Eckett, M. Sussman, and R. J. Jensen, "Coupled level-set/volume-of-fluid method for simulation of injector atomization," *J. Propul. Power* **29**(1), 147–157 (2013).
- ⁵⁴ X. Li and M. C. Soteriou, "High-fidelity simulation of fuel atomization in a realistic swirling flow injector," *Atomization Sprays* **23**(11), 1049–1078 (2013).
- ⁵⁵ M. Herrmann, "A parallel Eulerian interface tracking/Lagrangian point particle multi-scale coupling procedure," *J. Comput. Phys.* **229**(3), 745–759 (2010).
- ⁵⁶ X. Li and M. C. Soteriou, "HPC as a key enabler for high-fidelity simulation of liquid atomization in aerospace applications," in SciDAC 2011 Conference Proceedings, Denver, CO, 2011.
- ⁵⁷ X. Li, M. Arienti, M. C. Soteriou, and M. M. Sussman, "Towards an efficient, high-fidelity methodology for liquid jet atomization computations," AIAA Paper 2010-092407, 2010.
- ⁵⁸ M. Y. Leong and D. J. Hautman, "Near-field spray characterization of a liquid fuel jet injected into a crossflow," in ILASS Americas, 15th Annual Conference on Liquid Atomization and Spray Systems, Madison, WI, 2002.
- ⁵⁹ X. Li and M. C. Soteriou, "Validation of high-fidelity simulation of liquid jet atomization in crossflow," in ILASS Americas 27th Annual Conference on Liquid Atomization and Spray Systems, Raleigh, NC, 2015.
- ⁶⁰ X. Li and M. C. Soteriou, "Prediction of high density-ratio liquid jet atomization in crossflow using high fidelity simulations on HPC," in *50th AIAA Aerospace Sciences Meeting 2012, Nashville, Tennessee* (AIAA, 2012), p. 1138262.
- ⁶¹ M. Sussman, "A second order coupled level set and volume-of-fluid method for computing growth and collapse of vapor bubbles," *J. Comput. Phys.* **187**(1), 110–136 (2003).
- ⁶² A. S. Almgren *et al.*, "A conservative adaptive projection method for the variable density incompressible Navier–Stokes equations," *J. Comput. Phys.* **142**, 1–46 (1998).
- ⁶³ G. Falkovich, *Fluid Mechanics, a Short Course for Physicists* (Cambridge University Press, 2011).
- ⁶⁴ J. H. Lienhard, "Velocity coefficients for free jets from sharp-edged orifices," *J. Fluids Eng.* **106**, 13–17 (1984).
- ⁶⁵ R. K. Madabhushi, M. Y. Leong, M. Arienti, C. T. Brown, and V. G. McDonell, "On the breakup regime map of liquid jet in crossflow," in ILASS Americas, 19th Annual Conference on Liquid Atomization and Spray Systems, Toronto, Canada, 2006.
- ⁶⁶ K. A. Sallam and G. M. Faeth, "Surface properties during primary breakup of turbulent liquid jets in still air," *AIAA J.* **41**(8), 1514–1524 (2003).
- ⁶⁷ K. Lee, C. Aalburg, F. J. Diez, G. M. Faeth, and K. A. Sallam, "Primary breakup of turbulent round liquid jets in uniform crossflows," *AIAA J.* **45**(8), 1907–1916 (2007).
- ⁶⁸ E. Lubarsky, D. Shcherbak, O. Bibik, Y. Gopala, and B. T. Zinn, "Fuel jet in cross flow—Experimental study of spray characteristics," in *Advanced Fluid Dynamics* (InTech, 2012).
- ⁶⁹ M. Arienti, W. Pan, X. Li, and G. Karniadakis, "Many-body dissipative particle dynamics simulation of liquid/vapor and liquid/solid interactions," *J. Chem. Phys.* **134**, 204114 (2011).
- ⁷⁰ J. A. Schetz, E. A. Kush, and P. B. Joshi, "Wave phenomena in liquid jet breakup in a supersonic crossflow," *AIAA J.* **18**(7), 774–778 (1980).
- ⁷¹ S. L. Wang, Y. Huang, and Z. L. Liu, "Theoretical analysis of surface waves on a round liquid jet in a gaseous crossflow," *Atomization Sprays* **24**(1), 23–40 (2014).
- ⁷² N. F. El-Ansary, G. A. Hoshoudy, A. S. Abd-Elrady, and H. A. Ayyad, "Effects of surface tension and rotation on the Rayleigh–Taylor instability," *Phys. Chem. Chem. Phys.* **4**, 1464–1470 (2002).
- ⁷³ S. Chandrasekhar, *Hydrodynamic and Hydromagnetic Stability* (Dover, 1961).
- ⁷⁴ R. D. Reitz, "Modeling atomization processes in high-pressure vaporizing sprays," *Atomisation and Spray Technology* **3**, 309–337 (1987).
- ⁷⁵ P. Marmottant and E. Villermoux, "On spray formation," *J. Fluid Mech.* **498**, 73–111 (2004).
- ⁷⁶ T. v. Kármán, *Aerodynamics* (McGraw-Hill, 1963).